

Magnetically Regulated Star Formation in 3D: The Case of Taurus Molecular Cloud Complex

Fumitaka Nakamura¹ and Zhi-Yun Li²

ABSTRACT

We carry out three-dimensional MHD simulations of star formation in turbulent, magnetized clouds, including ambipolar diffusion and feedback from protostellar outflows. The calculations focus on relatively diffuse clouds threaded by a strong magnetic field capable of resisting severe tangling by turbulent motions and retarding global gravitational contraction in the cross-field direction. They are motivated by observations of the Taurus molecular cloud complex (and, to a lesser extent, Pipe Nebula), which shows an ordered large-scale magnetic field, as well as elongated condensations that are generally perpendicular to the large-scale field. We find that stars form in earnest in such clouds when enough material has settled gravitationally along the field lines that the mass-to-flux ratios of the condensations approach the critical value. Only a small fraction (of order 1% or less) of the nearly magnetically-critical, condensed material is turned into stars per local free-fall time, however. The slow star formation takes place in condensations that are moderately supersonic; it is regulated primarily by magnetic fields, rather than turbulence. The quiescent condensations are surrounded by diffuse halos that are much more turbulent, as observed in the Taurus complex. Strong support for magnetic regulation of star formation in this complex comes from the extremely slow conversion of the already condensed, relatively quiescent C¹⁸O gas into stars, at a rate two orders of magnitude below the maximum, free-fall value. We analyze the properties of dense cores, including their mass spectrum, which resembles the stellar initial mass function.

Subject headings: ISM: clouds — ISM: magnetic fields — MHD — stars: formation — turbulence

¹Faculty of Education, Niigata University, 8050 Ikarashi-2, Niigata 950-2181, Japan; fnakamur@ed.niigata-u.ac.jp

²Department of Astronomy, University of Virginia, P. O. Box 400325, Charlottesville, VA 22904; zl4h@virginia.edu

1. Introduction

Stars form in molecular clouds that are both turbulent and magnetized. The relative importance of the turbulence and magnetic field in controlling star formation is a matter of debate (McKee & Ostriker 2007). Early quantitative studies have concentrated on the formation and evolution of individual (low-mass) cores out of quiescent, magnetically supported clouds (Nakano 1984; Shu et al. 1987; Mouschovias & Ciolek 1999). Recent numerical simulations have focused more on the role of turbulence in the dynamics of larger clouds and core formation in them (as reviewed in, e.g., Mac Low & Klessen 2004). Ultimately, the debate must be settled by observations, especially direct measurements of the magnetic field strength in the bulk of the molecular gas, which are generally difficult to do (e.g., Heiles & Crutcher 2005). In the absence of such measurements, we have to rely on indirect evidence.

The best observed region of active star formation is arguably the nearby Taurus molecular cloud complex. Although it is not clear whether the complex is magnetically supported or not as a whole, the more diffuse regions are probably magnetically dominated. The strongest evidence comes from thin strands of ^{12}CO emission that are aligned with the directions of the local magnetic field (Heyer et al. 2008), as traced by polarization of background star light. The magnetic field in the strands is apparently strong enough to induce a measurable difference between the turbulent velocities along and perpendicular to the field direction. Heyer et al. concluded that the field strength is probably high enough to render the relatively diffuse striated region subcritical, with a magnetic flux-to-mass ratio greater than the critical value $2\pi G^{1/2}$ (Nakano & Nakamura 1978). The CO striations are strikingly similar to those observed in the nearby Riegel-Crutcher HI cloud, mapped recently by McClure-Griffiths et al. (2006), using 21cm absorption against the strong continuum emission towards the galactic center region. Its hair-like strands are also along the directions of the local magnetic field, again traced by the polarization vectors of the background star light. The authors estimated a field strength of $\sim 30 \mu\text{G}$ inside the strands. Kazes & Crutcher (1986) measured the line-of-sight field strength at a nearby location, and found $B_{los} \sim 18 \mu\text{G}$, which is consistent with the above estimate if a correction of ~ 2 is applied for projection effect. These are clear examples of magnetic domination in, respectively, cold HI and relatively diffuse molecular clouds.

It is unclear, however, how representative these two clouds are. In particular, the degree of magnetization is uncertain in giant molecular clouds (GMCs), where the majority of stars form. Elmegreen (2007) argued that the envelopes of GMCs, where most of the molecular gas resides, are probably magnetically critical or even subcritical, and can be long-lived if not for disruption by rapid star formation in GMC cores, which are probably supercritical, with internal dynamics dominated by turbulence; this supposition needs to be tested by

magnetic field observations on GMC scales (e.g., Novak, et al. 2007). Nevertheless, the Taurus cloud complex and the Riegel-Crutcher cloud are probably best mapped cloud in CO and HI, respectively. How such relatively diffuse, apparently magnetically dominated clouds proceed to condense and collapse to form stars is the focus of our paper.

Diffuse clouds are expected to condense more easily along than across the field lines as long as they are dominated by ordered large-scale magnetic fields. Such an anisotropic condensation can increase the density greatly with little corresponding increase in the magnetic field strength. This expectation is consistent with the available Zeeman measurements of field strength, which is more or less constant below a number density of order 10^3 cm^{-3} (Heiles & Crutcher 2005). Above this density, the field strength tends to increase with density, indicating that contraction perpendicular to the field lines becomes significant. We interpret the break in the observed field strength-density relation as marking the point where the self-gravity of the cloud becomes dynamically important in the cross-field direction. Before this point is reached, one expects the self-gravity to first become significant along the field lines (where there is no magnetic support), pulling matter into condensations, which can be either a sheet, a filament, or even a knot, depending on the degree of anisotropy in the initial mass distribution.

In the case of the Taurus molecular cloud complex, most of the dense molecular gas traced by ^{13}CO and especially C^{18}O are distributed in structures elongated more or less perpendicular to the large-scale magnetic field (e.g., Onishi et al. 1996, 2002; Goldsmith et al. 2008). It has long been suspected that they have condensed along the field lines (e.g., Heyer et al. 1987; Tamura et al. 1987). Cross-field contraction must have already taken place in the condensed structures, at least locally, since stars have been forming in these structures for at least a few million years (Kenyon & Hartmann 1995). Palla & Stahler (2002) examined the star formation pattern in the Taurus clouds in both space and time, concluding that stars began to form at a low level at least 10 million years ago, in a spatially dispersed fashion. The majority of the stars are formed, however, in the last 3 million years, near where the dense gas is observed today. This pattern of accelerating star formation is precisely what is expected of a magnetically dominated cloud that condenses in two stages: first along the field line, when little star formation is expected, except perhaps in some pockets that have an exceptionally weak local magnetic field to begin with or have their magnetic fluxes reduced by an exceptionally strong compression-enhanced ambipolar diffusion, and then across the field, when more active star formation can take place throughout the dense sheets and filaments that have condensed along the field lines. A strong support for this supposition comes from the fact that star formation is slow even in dense gas: the rate of star formation for the last 3 million years is about $\dot{M}_* \sim 5 \times 10^{-5} M_\odot \text{yr}^{-1}$ (Goldsmith et al. 2008), two orders of magnitude below the free-fall rate for the dense ($\sim 10^4 \text{ cm}^{-3}$) C^{18}O gas (Onishi et al.

2002; see § 6.2.1 for actual numbers); Krumholz & Tan (2006) found that a similar result holds for objects of a wide range of density. Although the observed moderately supersonic motions ($\mathcal{M} \sim 2$) can provide some support for the dense gas, we believe that the star formation is slow mainly because the bulk of the dense gas remains magnetically supported even after cross-field contraction has begun in localized regions in the condensed structures. This requirement can naturally be satisfied if such structures are marginally magnetically critical (Basu & Ciolek 2000), where individual stars can form on a relatively short time scale, but the overall rate of star formation remains well below the free-fall value, as we have demonstrated using simulations in 2D sheet-like geometry (Li & Nakamura 2004 and Nakamura & Li 2005; LN04 and NL05 hereafter; see also Kudoh et al. 2007 and Kudoh & Basu 2008). The Taurus cloud complex is discussed further in § 6.2.1, along with the Pipe Nebula (§ 6.2.2), which may represent an earlier phase of star formation in a magnetically dominated cloud (Lada et al. 2008; F. Alves et al., in preparation).

The rest of the paper is organized as follows. Section 2 describes the model formulation, including governing equations, initial and boundary conditions, and numerical code. It is followed by three sections on numerical results. Section 3 concentrates on a standard model with a particular combination of initial turbulence and outflow feedback. It illustrates the essential features of the magnetically regulated star formation in three dimensions, including strong stratifications in density and turbulent speed, broad probability distribution functions (PDFs) of volume and column densities and, most importantly, low rate of star formation. This model is contrasted, in § 4, with others that have different levels of initial turbulence and outflow feedback. We devote § 5 to a detailed analysis of dense cores, including their shapes, mass spectrum, velocity dispersions, flux-to-mass ratios, angular momenta, and whether they are bound or not. In § 6, we outline a general scenario of magnetically regulated star formation in quiescent condensations of relatively diffuse, turbulent clouds, and make connection to observations of the Taurus molecular cloud complex and Pipe Nebula. The main results of the paper are summarized in § 7. Readers interested only in the general scenario and their connection to observations can skip to § 6.

2. Model Formulation

2.1. Governing Equations

The basic equations that govern the evolution of isothermal, weakly ionized, magnetized molecular gas are (see, e.g., Shu 1991)

$$\frac{\partial \rho_n}{\partial t} + \nabla \cdot (\rho_n \mathbf{V}_n) = 0 , \quad (1)$$

$$\rho_n \frac{\partial \mathbf{V}_n}{\partial t} + \rho_n (\mathbf{V}_n \cdot \nabla \mathbf{V}_n) = -\rho_n \nabla \Psi - c_s^2 \nabla \rho_n + \frac{1}{4\pi} (\nabla \times \mathbf{B}) \times \mathbf{B} , \quad (2)$$

$$\frac{\partial \mathbf{B}}{\partial t} = \nabla \times (\mathbf{V}_i \times \mathbf{B}) , \quad (3)$$

$$\nabla^2 \Psi = 4\pi G \rho_n , \quad (4)$$

where ρ , \mathbf{V} , \mathbf{B} , c_s , and Ψ are, respectively, density, velocity, magnetic field, isothermal sound speed, and gravitational potential, with the subscripts n and i denoting neutrals and ions. The drift velocity between ion and neutral is

$$\mathbf{V}_i - \mathbf{V}_n = \frac{t_c}{4\pi\rho_n} (\nabla \times \mathbf{B}) \times \mathbf{B} , \quad (5)$$

where the coupling time between the magnetic field and neutral matter, t_c , is given by

$$t_c = \frac{1.4}{\gamma C \rho_n^{1/2}} , \quad (6)$$

in the simplest case where the coupling is provided by ions that are well tied to the field lines and the ion density ρ_i is related to the neutral density by the canonical expression $\rho_i = C \rho_n^{1/2}$. We adopt an ion-neutral drag coefficient $\gamma = 3.5 \times 10^{13} \text{ cm}^3 \text{ g}^{-1} \text{ s}^{-1}$ and $C = 3 \times 10^{-16} \text{ cm}^{-3/2} \text{ g}^{1/2}$ (Shu 1991). The factor 1.4 in the above equation comes from the fact that the cross section for ion-helium collision is small compared to that of ion-hydrogen collision (Mouschovias & Morton 1991). These governing equations are solved numerically subject to a set of initial and boundary conditions.

2.2. Initial and Boundary Conditions

Our simulations are carried out in a cubic box (of size L), with standard periodic conditions imposed at the boundaries. The cloud is assumed to have a uniform density ρ_0 initially. The corresponding Jeans length is

$$L_J = (\pi c_s^2 / G \rho_0)^{1/2} , \quad (7)$$

where the isothermal sound speed $c_s = 1.88 \times 10^4 (T/10K)^{1/2} \text{ cm/s}$, with T being the cloud temperature. The initial density $\rho_0 = 4.68 \times 10^{-24} n_{H_2,0} \text{ g cm}^{-3}$, where $n_{H_2,0}$ is the initial number density of molecular hydrogen, assuming 1 He for every 10 H atoms.

We consider relatively diffuse molecular clouds, with a fiducial H_2 number density of 250 cm^{-3} . It is the value adopted by Heyer et al. (2008) for the sub-region in Taurus that shows magnetically aligned ^{12}CO striations. Scaling the density by this value, we have

$$L_J = 1.22 \left(\frac{T}{10K} \right)^{1/2} \left(\frac{n_{H_2,0}}{250 \text{ cm}^{-3}} \right)^{-1/2} \text{ pc} , \quad (8)$$

and a Jeans mass

$$M_J = \rho_0 L_J^3 = 31.6 M_\odot \left(\frac{T}{10K} \right)^{3/2} \left(\frac{n_{H_2,0}}{250 \text{ cm}^{-3}} \right)^{-1/2}. \quad (9)$$

The Jeans length is smaller than the dimensions of molecular cloud complexes such as the Taurus clouds, which are typically tens of parsecs. Although global simulations on the complex scale are desirable, they are prohibitively expensive if individual star formation events are to be resolved at the same time. After some experimentation, we settled on a moderate size for the simulation box, with an initial Jeans number $n_J = L/L_J = 2$. It represents a relatively small piece of a larger complex. Scaling the Jeans number by 2, we have a box size

$$L = 2.44 \left(\frac{n_J}{2} \right) \left(\frac{T}{10K} \right)^{1/2} \left(\frac{n_{H_2,0}}{250 \text{ cm}^{-3}} \right)^{-1/2} \text{ pc}, \quad (10)$$

and a total mass

$$M_{tot} = 253 M_\odot \left(\frac{n_J}{2} \right)^3 \left(\frac{T}{10K} \right)^{3/2} \left(\frac{n_{H_2,0}}{250 \text{ cm}^{-3}} \right)^{-1/2} \quad (11)$$

in the computation domain. Even though the initial Jeans number adopted is relatively small, there is enough material inside the box to form many low-mass stars, especially in condensations where the Jeans mass is much reduced.

We impose a uniform magnetic field along the x axis at the beginning of simulation. The field strength B_0 is specified by the parameter α , the ratio of magnetic to thermal pressure, through

$$B_0 = 3.22 \alpha^{1/2} \left(\frac{T}{10K} \right)^{1/2} \left(\frac{n_{H_2,0}}{250 \text{ cm}^{-3}} \right)^{1/2} (\mu G). \quad (12)$$

In units of the critical value $2\pi G^{1/2}$ (Nakano & Nakamura 1978), the flux-to-mass ratio for the material inside the box is

$$\Gamma_0 = 0.45 n_J^{-1} \alpha^{1/2}. \quad (13)$$

Since we are interested in magnetic regulation of star formation, we choose a relatively strong magnetic field with $\alpha = 24$, corresponding to a mildly magnetically subcritical region with $\Gamma_0 = 1.1$ (or a dimensionless mass-to-flux ratio $\lambda = 0.91$) for $n_J = 2$, which is close to the value of 1.2 used in the 2D simulations of LN04 and NL05. For the fiducial values for temperature and density, the initial field strength is $B_0 = 15.8 \mu\text{G}$ according to equation (12); this value is not unreasonably high (see § 6.2.1 for a discussion of the magnetic field in the Taurus region). We postpone an investigation of initially supercritical clouds to a future publication.

Molecular clouds are highly turbulent, particularly for the relatively diffuse gas that we have assumed for the initial state. It is established that supersonic turbulence decays rapidly, with or without a strong magnetic field (e.g., Mac Low & Klessen 2004). How the turbulence is maintained is uncertain (e.g., McKee & Ostriker 2007). For the relatively small, parsec-scale region that is modeled here, a potential source is energy cascade from larger scales, which can in principle keep the turbulence in the sub-region for a time longer than the local crossing time. Ideally, this (and may other) form of driving should be included in a model, although it is unclear how this can be done in practice. We will take the limit that the turbulence decays freely, except for the feedback from protostellar outflows that are associated with forming stars. Other forms of driving will be considered elsewhere. Following the standard practice (e.g., Ostriker et al. 2001), at the beginning of the simulation ($t = 0$) we stir the cloud with a turbulent velocity field of power spectrum $v_k^2 \propto k^{-3}$ in Fourier space.

A useful time scale for cloud evolution is the global gravitational collapse time (Ostriker et al. 2001)

$$t_g = \frac{L_J}{c_s} = 6.36 \times 10^6 \left(\frac{n_{H_2,0}}{250 \text{ cm}^{-3}} \right)^{-1/2} \text{ (years)}, \quad (14)$$

which is longer than the free-fall time at the initial density, $t_{ff,0} = [3\pi/(32G\rho_0)]^{1/2}$, by a factor of 3.27. In the presence of a strong magnetic field, as is the case in our simulation, gravitational condensation is expected to occur preferentially along field lines, creating a flattened, sheet-like, structure in which most star formation activities take place. Inside the sheet, the characteristic Jeans length is

$$L_s \equiv \frac{c_s^2}{G\Sigma_0} = \frac{1}{\pi n_J} L_J = 0.195 \left(\frac{2}{n_J} \right) \left(\frac{T}{10K} \right)^{1/2} \left(\frac{n_{H_2,0}}{250 \text{ cm}^{-3}} \right)^{-1/2} \text{ pc}, \quad (15)$$

corresponding to a local gravitational collapse time

$$t_s \equiv \frac{L_s}{c_s} = \frac{c_s}{G\Sigma_0} = \frac{1}{\pi n_J} t_g = 1.01 \times 10^6 \left(\frac{2}{n_J} \right) \left(\frac{n_{H_2,0}}{250 \text{ cm}^{-3}} \right)^{-1/2} \text{ (years)}, \quad (16)$$

where the column density Σ_0 is measured along the initial magnetic field lines, $\Sigma_0 = \rho_0 L = n_J \rho_0 L_J$. The sheet has a Jeans number $n_s \equiv L/L_s = \pi n_J^2$, corresponding to 12.6 for $n_J = 2$, which is close to the value of 10 adopted in the 2D simulations of LN04 and NL05. Note that the gravitational collapse time t_s is longer than the free-fall time of the condensed sheet

$$t_{ff,s} = \left(\frac{3\pi}{32G\rho_s} \right)^{1/2}, \quad (17)$$

by a factor of 2.31, where the characteristic sheet density is given by

$$\rho_s = \frac{\pi G \Sigma_0^2}{2c_s^2} = \frac{\pi^2 n_J^2}{2} \rho_0. \quad (18)$$

2.3. Numerical Code

We solve the equations that govern the cloud evolution using a 3D MHD code based on an upwind TVD scheme, with the $\nabla \cdot \mathbf{B} = 0$ condition enforced through divergence cleaning after each time step. The base code is the same as the one used in the cluster formation simulations of Li & Nakamura (2006) and Nakamura & Li (2007), except that we have now included ambipolar diffusion in the induction equation. The ambipolar diffusion term is treated explicitly, which puts a stringent requirement on the time step (since it is proportional to the square of the grid size, Mac Low et al. 1995), especially in the lowest density regions. To alleviate the problem, we set a density threshold, $\rho_{AD} = 0.1\rho_0$, below which the rate of ambipolar diffusion is reduced to zero. A similar approach was taken by Kudoh et al. (2007), and can be justified to some extent by increased ionization of low (column) density gas from UV background (McKee 1989). Even with this measure, it still takes more than a month to run a standard 128^3 simulation for two global gravitational collapse time t_g (or 4π times the sheet collapse time t_s) on the vector machine available to us. Since our focus is on the evolution of, and star formation in, the condensed gas sheet, to speed up the simulations, we follow the initial phase of cloud evolution on a coarser grid of 64^3 up to a maximum density of $\sim 40 \rho_0$, before switching to the 128^3 grid. To gauge the numerical diffusion of magnetic field on such a relatively coarse grid, we have followed the evolution of a model cloud in the ideal MHD limit (with the ambipolar diffusion term turned off; Model I0 in Table 1) up to $2t_g (= 12.6t_s)$, and found that the mass-to-flux ratio is conserved to within 1.5%, which seems to be much better than the two-dimensional higher resolution runs with ZEUS (512^3 , Krasnopolsky & Gammie 2005).

A difficulty with grid-based numerical codes such as ours in simulating star formation in turbulent clouds is that, once the collapse of a piece of the cloud runs away to form the first star, the calculation grinds to a halt without special treatment. Because the bulk of the stellar mass is believed to be assembled over a rather brief (Class 0) phase of $\sim 3 \times 10^4$ yrs (Andre et al. 1993) and the outflows are most active during this phase (much shorter than the fiducial characteristic time $t_s \sim 10^6$ yrs), we idealize the processes of individual star formation and outflow ejection as instantaneous, and treat them using the following simple prescriptions. When the density in a cell reaches a threshold value $\rho_{th} = 10^3 \rho_0$, we define around it a critical core using a version of CLUMPFIND algorithm (Williams, de Geus, & Blitz 1994; see § 5 for detail). The core identification routine is specified by a minimum threshold density $\rho_{th,min}$ and the number of density levels N . They are set to $200 \rho_0$ and 5 respectively. The mean density of the core so identified is estimated at $\sim 10^5 \text{ cm}^{-3}$, comparable to those of H^{13}CO^+ cores in Taurus studied by Onishi et al. (2002). We extract 30% of the mass from the core (if its mass exceeds the local Jeans mass), and put it in a Lagrangian particle located at the cell center; its subsequent evolution is followed using the

standard leap-frog method. The extracted mass fraction is motivated by the observations of J. Alves et al. (2007), who found a mass spectrum for dense cores that is similar to the stellar IMF in shape but more massive by a factor of ~ 3 (see also Ikeda, Sunada, & Kitamura 2007). It is within the range of 25 – 75% for the star formation efficiency per dense core estimated theoretically by Matzner & McKee (2000).

The material remaining in the core after mass extraction is assumed to be blown away in a two-component outflow: a bipolar jet of 30° half-opening angle around the local magnetic field direction that carries a fraction η of the total momentum, and a spherical component outside the jet that carries the remaining fraction. The total outflow momentum is assumed to be proportional to the stellar mass, with a proportionality coefficient of $P_* = 35$ km/s. The prescriptions for star formation and outflow are similar to those used in Nakamura & Li (2007). One difference is the use of CLUMPFIND here to define the critical core. Another is that, when an outflow reenters the computation box because of periodic boundary condition, we reduce its strength by a factor of ten if its speed exceeds $50 c_s$, to prevent it from strongly perturbing or even disrupting the condensed sheet.

3. Standard Model

We have run four models that include ambipolar diffusion, with parameters listed in Table 1. They differ in random realization of the initial velocity field, relative strength of the jet and spherical outflow components, and level of initial turbulence. An ideal MHD run was also performed for comparison. In this section, we focus on the model with initial turbulent Mach number $\mathcal{M} = 3$ and jet momentum fraction $\eta = 75\%$. It serves as the standard against which other models, to be discussed in the next section, are compared.

The initial phase of cloud evolution is similar to those already presented in Krasnopolsky & Gammie (2005), who carried out high-resolution, ideal MHD simulations of magnetically subcritical clouds in two dimensions, including self-gravity and an initially supersonic turbulence that decays freely, as in our simulation. The initial turbulence creates many shocklets that are oriented more or less perpendicular to the field lines; they appear as filaments of enhanced density and are the main sites of turbulence dissipation. As the turbulence decays, the fragments start to coalesce, eventually forming a single, approximate Spitzer sheet. In the ideal MHD limit, the sheet formation marks the end of cloud evolution. With ambipolar diffusion, it signals the beginning of a new phase—star formation¹. This latter phase is the

¹For a strong enough turbulence and/or initially inhomogeneous distribution of mass-to-flux ratio, stars can form before the formation of a well-defined sheet (see § 6 for further discussion).

focus of our discussion next.

3.1. Star Formation Efficiency

We begin the discussion with a global measure of star formation in the standard model: the efficiency of star formation, defined as the ratio of the mass of all stars to the total mass of stars and gas. The star formation efficiency (SFE hereafter) is plotted in Fig. 1 as a function of time in units of the gravitational collapse time of the sheet t_s . Sheet formation is finished by the end of the first global collapse time $t_g = 2\pi t_s$. Soon after, the first star appears, around $t \approx 7 t_s$. By the end of simulation at $t = 11.4 t_s$ (nearly $2 t_g$), 37 stars have formed, yielding an accumulative SFE of 6.5%. The average mass of a star is close to $0.45 M_\odot (T/10K)^{3/2} (n_{H_2,0}/250\text{cm}^{-3})^{-1/2}$, typical of low-mass stars. The rate of star formation is given by the slope of the SFE curve, which is estimated at $\sim 1.5\%$ per t_s . At this rate, it would take $\sim 65 t_s$ to deplete the gas due to star formation. The gas depletion time corresponds to $\sim 10 t_g$ or ~ 33 times the free-fall time $t_{\text{ff},0}$ at the *initial* (uniform) density ρ_0 . In other words, the star formation efficiency per *initial* free fall time (Krumholz & McKee 2005) is $\text{SFE}_{\text{ff},0} \sim 3\%$. Interestingly, this rate is comparable to that of cluster formation in protostellar outflow-driven turbulence (Nakamura & Li 2007). However, a large fraction of the gas is at a much higher density than the initial density ρ_0 after the formation of the condensed sheet. It is more appropriate to measure the star formation rate using the free fall time at the characteristic sheet density $\rho_s = 2\pi^2 \rho_0$, which is $t_{\text{ff},s} = 0.43 t_s$ (see equation [17]), yielding $\text{SFE}_{\text{ff},s} \sim 0.7\%$. To help understand the rather slow and inefficient star formation, we next examine in some detail the cloud structure and dynamics at $t = 11 t_s$, representative of the post-sheet formation phase of cloud evolution when stars are forming steadily, starting with overall mass distribution as revealed by column density.

3.2. Column Density Distribution

The cloud material is expected to condense along the magnetic field lines into a flattened structure. This expectation is borne out by Figs. 2 and 3, which show the distributions of column density along, respectively, the y - and x -axis (the direction of the initial magnetic field). Viewed edge-on, the structure resembles a knotty, wiggly filament (Fig. 2). The dense filament is sandwiched by a low-density “halo,” which contains a number of spurs more or less perpendicular to the filament. The spurs are roughly aligned with the global magnetic field. They resemble the diffuse, fuzzy ^{12}CO streaks that are frequently observed to stream away from dense filaments (Goldsmith et al. 2008). Similar spurs are seen in the recent

SPH-MHD simulations of Price & Bate (2008).

The face-on view of the condensed structure is quite different (Fig. 3). It appears highly fragmented, with low-density voids as well as high-density peaks. Some over-dense regions cluster together to form a short filament; others are more scattered. The actual appearance of the cloud to outside observers will depend, of course, on the viewing angle. It can be filament-like (as in Fig. 2) or, more likely, patchy (as in Fig. 3). Superposed on the face-on column density map is the distribution of the 33 stars that have formed up to the time plotted. With few exceptions, they follow the dense gas closely. Most of the stars are found in small groups, which is broadly consistent with the distribution of young stars in Taurus (Gomez et al. 1993). Since the clouds is initially magnetically subcritical everywhere, in order for any localized region to collapse and form stars, it must become supercritical first.

A rough measure of magnetic criticality is provided by the average mass-to-flux ratio $\bar{\lambda}$ normalized to the critical value,

$$\bar{\lambda}(y, z) = \int_{-L/2}^{+L/2} 2\pi G^{1/2} \rho / B_x dx. \quad (19)$$

Contours of $\bar{\lambda} = 1$ are plotted in Fig. 3, showing that most of the dense regions are indeed magnetically supercritical, and thus capable of forming stars in principle. The supercritical regions enclosed within the contours contain a significant fraction (34%) of the total mass. The mass fraction of supercritical gas increases gradually with time initially, and remains more or less constant at later times ($t \gtrsim 6 t_s$), as shown in Fig. 4. This value provides an upper limit to the efficiency of star formation. If the supercritical regions collapse to form stars within a local free fall time, the star formation rate would be much higher than the actual value. An implication is that the bulk of the supercritical material remains magnetically supported to a large extent and is rather long lived. Only its densest parts (i.e., dense cores), which contain a small fraction of the supercritical mass, directly participate in star formation at any given time. The longevity is characteristic of the (mildly) supercritical regions that are produced through turbulence-accelerated ambipolar diffusion in nearly magnetically critical clouds. It is in contrast with the highly supercritical material in weakly magnetized clouds, which is expected to collapse promptly unless supported by turbulence. This same behavior was found in 2D calculations (NL05).

To quantify the mass distribution further, we plot in Fig. 5 the probability distribution function (PDF) of the column density along the x -axis, in the direction of initial magnetic field. The PDF peaks around $\Sigma \sim 1.7 \rho_0 L_J$ (where ρ_0 and L_J are the density and Jeans length of the initial, uniform state), close to the average value of $2 \rho_0 L_J$. The distribution can be described reasonably well by a lognormal distribution, although there is significant deviation at both low and high density end. The considerable spread in column density may

be surprising at the first sight, since one may expect little structure to develop in a subcritical sheet dominated by a strong, more or less uniform magnetic field, especially since the initial mass distribution is also chosen to be uniform. This expectation is consistent with the column density PDF of the ideal MHD counterpart of the standard model (plotted in the same figure for comparison), which is much narrower. The key difference is that ambipolar diffusion turns an increasingly large fraction of the initially subcritical cloud into supercritical material (until saturation sets in at late times, see Fig. 4). Once produced, the supercritical material behaves drastically differently from the subcritical background. It is easier to compress by an external flow because its magnetic field is weaker. The compressed supercritical region also rebounds less strongly, because the magnetic forces driving the rebound are cancelled to a larger extent by the self-gravity of the region. More importantly, the supercritical regions can further condense without external compression, via self-gravity. The accumulation of supercritical material and subsequent (magnetically-diluted) gravitational fragmentation in such material are responsible for the broad column density PDF. These key aspects of the problem are *not* captured by the ideal MHD simulation, but are well illustrated in 2D simulations that include ambipolar diffusion (e.g., NL05; Kudoh & Basu 2006). Other aspects are better discussed in 3D, however. These include the dependence of various physical quantities on volume density, to which we turn our attention next.

3.3. Density Stratification

Our model cloud is strongly stratified in density. It contains dense cores embedded in a condensed sheet which, in turn, is surrounded by a more diffuse halo. The relative amount of mass distributed at different densities is displayed in Fig. 6, along with that for the ideal MHD case and for a Spitzer sheet. Whereas the mass distribution for the ideal MHD case resembles that of the Spitzer sheet closely, the same is not true for the standard model with ambipolar diffusion: its mass distribution is considerably broader, with more material at both the low and high density end. The former indicates that the diffuse material outside the sheet is dynamically active, as we show below. The excess at the high density end is produced, on the other hand, primarily by ambipolar diffusion, which enables pockets of the sheet material to condense across magnetic field lines gravitationally. The bulk (62.5%) of the cloud material resides in the condensed sheet, which we define somewhat arbitrarily as the material in the density range between $5 \rho_0$ and $50 \rho_0$, corresponding to a range in H_2 number density between $1.25 \times 10^3 \text{ cm}^{-3}$ and $1.25 \times 10^4 \text{ cm}^{-3}$ (assuming $n_{H_2,0} = 250 \text{ cm}^{-3}$). The remaining cloud material is shared between the diffuse halo (30.0%), defined loosely as the material with density below $5 \rho_0$, and dense cores (7.5%), defined as the material denser than $50 \rho_0$ (see § 5 below).

Our model cloud is also strongly stratified in turbulent speed. Fig. 7 shows the mass weighted rms velocity as a function of density. At densities corresponding to the condensed sheet ($5 - 50 \rho_0$), the turbulent Mach number is about 2. The moderately supersonic turbulence persists in the condensed sheet for many local free fall times, despite the absence of external driving. It is driven by a combination of outflows (through either direct impact or MHD waves) and ambipolar diffusion-induced gravitational acceleration. The modest increase in rms velocity toward the high density end is because the denser gas is typically closer to star forming sites and is thus more strongly perturbed by outflows. The much higher level of turbulence in the diffuse halo is more intriguing. One may expect little turbulence to remain at the representative time $t = 11 t_s$ shown in the figure, which is well beyond the time ($t \sim 6 t_s$) of sheet formation — a product of turbulence dissipation. The expectation is consistent with the ideal MHD simulation, which shows that, in the absence of external driving, the turbulent motions die down quickly everywhere. The turbulence decay is changed by ambipolar diffusion which, accelerated by the initial strong turbulence, enables stars to form soon after sheet formation. The stars stir up the halo via protostellar outflows in at least two ways. First, the outflows are powerful enough to disrupt the star-forming cores, break out from the condensed sheet, and inject energy and momentum directly into the halo. Second, a fraction of the outflow energy and momentum is also deposited in the sheet, where gas motions can shake the field lines and send into the halo MHD waves whose amplitudes grow as the density decreases (Kudoh & Basu 2003); the waves help maintain the turbulence in the diffuse region, particularly in the cross-field direction.

Even though the turbulence speed is relatively high in the halo, it is still sub-Alfvénic. This is shown in Fig. 8, where the average Alfvén Mach number M_A is plotted as a function of density. The flow is moderately sub-Alfvénic at densities between ~ 0.3 and $\sim 10 \rho_0$, with M_A within 20% of 0.5. The Alfvén Mach number drops slowly towards lower densities, indicating that the lower-density gas becomes increasingly more magnetically dominated in our model cloud. A caveat is that, in real clouds such as the Taurus complex, the dynamics of the low-density halo on the parsec-scale of our modeled region are expected to be tied to that of the larger complex. It is likely for the diffuse gas to receive energy cascaded from larger scales and become more turbulent than suggested by Fig. 8. Some of this energy may even be fed through Alfvén waves into the condensed sheet and increase its velocity dispersion as well. The increase is not expected to be large, however, since the Alfvén speed becomes transonic at high densities (see Fig. 8), where highly supersonic motions should damp out quickly through shock formation. In future refinements, it will be desirable to include external driving of the halo material, which may modify the way stars form, especially at early times (see discussion in § 6). Nevertheless, we believe that the decrease of turbulent speed with increasing density found in our simulation (and earlier in Kudoh & Basu 2003)

is a generic feature of the magnetically regulated star formation in three dimensions. It is broadly consistent with the observed trend (e.g., Myers 1995).

Another generic feature is the distribution of magnetic field strength as a function of density. The distribution is shown in Fig. 9. There is a clear trend for the average field strength to remain more or less constant at relatively low densities, before increasing gradually towards the high density end. A similar trend is inferred in Zeeman measurements of field strength over a wide range of densities, and has been interpreted to mean that the initial stage of cloud condensation leading to star formation is primarily along the field lines, which increases the density without increasing the field strength (Heiles & Crutcher 2005). This is precisely what happens in our model, where the initial accumulation of diffuse material into the condensed sheet is mostly along the field lines, and further condensation inside the sheet is primarily in the cross-field direction. The cross-field condensation leads to an increase in field strength with density, although by a factor that is less than that expected from flux-freezing because of ambipolar diffusion.

3.4. Sheet Fragmentation: Turbulent or Gravitational?

The star formation activities in our model are confined mostly to the condensed sheet. Its dynamics hold the key to understanding the magnetically regulated star formation. An overall impression of the sheet can be gained from Figs. 2 and 3, which showed an edge-on and face-on view of the sheet in column density. The sheet has a highly inhomogeneous mass distribution which is, of course, a pre-requisite for active star formation. To illustrate the clumpy mass distribution further, we plot in Fig. 10 the distribution of the density in the “mid-plane” of the sheet, defined as the yz plane (perpendicular to the initial magnetic field along the x axis) that passes through the minimum of gravitational potential. The density distribution spans seven orders of magnitude, from $10^{-4} \rho_0$ (the density floor adopted in the computation) to $10^3 \rho_0$ (the threshold for Lagrangian particle generation). The question is: how is the density inhomogeneity created and maintained?

A widely discussed possibility is turbulent fragmentation, where regions of high densities are created by converging flows (e.g., Padoan & Nordlund 2002; Mac Low & Klessen 2004). There is indeed a random velocity field in the mid-plane, as shown by arrows in the figure. However, the flow speed is typically small, comparable to the sound speed in most places. It is unlikely for such a weak turbulence to create the high density contrast shown in Fig. 10 by itself. This conclusion is strengthened by the presence of a strong magnetic field, which cushions the flow compression. Indeed, the turbulent speeds in the plane of the sheet are significantly below the approximate magnetosonic speed $v_{ms} = [B_x^2/(4\pi\rho) + c_s^2]^{1/2}$ in most

places, and are thus not expected to create large density fluctuations; they are essentially a collection of magnetosonic waves. The low level of turbulence points to gravity rather than flow motions as the primary driver of fragmentation in the sheet.

Gravity is expected to be dynamically important in the sheet, a structure formed by gravitational condensation along field lines in the first place. The fact that the sheet has a dimension much larger than the thickness indicates that it contains many thermal Jeans masses. If the thermal pressure gradient was the main force that opposes the gravity, one would expect the bulk of the sheet to collapse in one gravitational time t_s . And yet, the vast majority of the sheet material remains uncollapsed after at least $\sim 5 t_s$. The longevity indicates that the gravitational fragmentation proceeds at a much reduced rate. The reduction is due, of course, to magnetic forces, which cancel out the gravitational forces in the plane of the sheet to a large extent (Shu & Li 1997, Nakamura et al. 1999). The near cancellation can be inferred from Fig. 10, where contours of gravitational potential are plotted along with the density and velocity vectors. If the gravitational forces were unopposed, one would expect the material to slide down the potential well, and picking up speed towards the bottom, with the infall speed reaching highly supersonic values. For example, for a potential drop of $8 c_s^2$ (say between contours labeled “–8” and “–16”), an increase in speed by $4 c_s$ is expected. These expectations are not met. The actual velocity field appears quite random, and generally transonic. The slow random motions in a rather deep gravitational potential well provide a clear indication for magnetic regulation of the sheet dynamics. Active outflows also play an important role in generating the density inhomogeneities observed in the condensed sheet. Their effects are discussed in § 4.2 below.

3.5. Comparison to 2D Calculations

There are a number of differences between the 3D simulation and the previous 2D calculations. The 2D treatment does not account for the mass stratification along the field lines, and thus cannot address the important issue of dynamical coupling between the condensed material and the diffuse halo. A related difference is that, in 3D, there is an initial phase of mass settling to form the sheet, which is absent in 2D. Furthermore, the mass of each star in the 2D models is held fixed (typically at $0.5 M_\odot$); in 3D, it is fixed at 30% of the mass of the critical core that forms the star. In addition, the prescription for outflow ² and the

²We note that the spherical component of the outflow in the standard 3D model carries a momentum close to (within 15% of) that of the 2D outflow in the plane of mass distribution in the standard model of NL05.

degree of initial cloud magnetization are also somewhat different. Despite these differences, the results of the 2D and 3D models are in remarkably good agreement.

The most important qualitative agreement is that, once settled along the magnetic field lines, the condensed sheet material produces stars at a slow rate. In the standard 2D model of NL05, about 5.3% of the total mass is converted into stars within a time interval of $3.35 t_s$ (see their Fig. 1), corresponding to a star formation rate of $\sim 1.6\%$ per sheet gravitational collapse time t_s . This rate is nearly identical to the value of $\sim 1.5\%$ estimated in § 3.1 for the standard 3D model (which is also close to that of the 3D $\mathcal{M} = 10$ model, see § 4 below). The (face-on) mass distributions are also similar in 2D and 3D models. In both cases, dense, star-forming cores are embedded in moderately supercritical filaments which, in turn, are surrounded by more diffuse, magnetically subcritical material (compare Fig. 3 with the lower panels of Fig. 2 of NL05). More quantitatively, the mass fraction of supercritical material increases gradually initially and reaches a plateau of $\sim 30\%$ in both 2D and 3D models. The similarity extends to the turbulent speed of the condensed material, which is about twice the sound speed in both cases at late times (see Fig. 7 and Fig. 11 of NL05).

The similarities indicate that 2D calculations capture the essence of the slow, magnetically regulated star formation in moderately subcritical clouds. The same conclusion was drawn by Kudoh et al. (2007) based on 3D simulations of weakly perturbed magnetically subcritical sheets. The 2D calculations have the advantage of being much faster to perform. They can be done with higher spatial resolution (512^2 as compared to the 128^3 used in this paper) and in larger numbers. The number of 3D simulations is necessarily more limited, especially because of the small time step required by our treatment of ambipolar diffusion using an explicit method. Nevertheless, we are able to perform several additional simulations, to check the robustness of the standard model, and to help elucidate the effects of two key ingredients: initial turbulence and outflow feedback.

4. Other Models

4.1. Initial Turbulence

Even though the initial turbulence dissipates quickly, it seeds inhomogeneities in mass distribution and mass-to-flux ratio that are expected to affect star formation later on. To illustrate the effects of initial turbulence, we focus on a model identical to the standard model, except for a higher initial turbulent Mach number $\mathcal{M} = 10$ (instead of 3). The overall pattern of cloud evolution follows that seen in the standard model: dissipation of turbulence leads to gravitational settling of cloud material onto a condensed sheet, the densest parts of

which collapse to form stars; the stars, in turn, stir up the sheet and its surrounding halo through protostellar outflows. One difference is that the stronger turbulence initiates star formation at an earlier time, as seen in Fig. 11. The first star forms around $\sim 4.5 t_s$ in the $\mathcal{M} = 10$ case, compared to $\sim 6.8 t_s$ for $\mathcal{M} = 3$. Nevertheless, their rates of star formation are comparable, with values between $\sim 0.5\%$ and $\sim 1.0\%$ per free fall time $t_{ff,s} = 0.43 t_s$ in both cases. The earlier start, but still low rate, of star formation in the more turbulent case is consistent with the turbulence-accelerated, magnetically regulated scenario that we advocate based on previous 2D calculations (LN04, NL05; see also recent 3D simulations of Kudoh & Basu 2008).

The basic structure and kinematics of the initially more turbulent cloud are also similar to those of the standard model cloud. In both cases, the condensed sheet is highly fragmented but dynamically “cold,” with moderately supersonic random motions. It is surrounded by a halo moving at highly supersonic, but sub-Alfvénic, speeds. An interesting difference is that the sheet in the $\mathcal{M} = 10$ case appears thicker, as illustrated in Fig. 12, where an edge-on view of the column density distribution (along the y -axis, perpendicular to the initial magnetic field direction) is plotted for a representative time $t = 8 t_s$. It is to be compared with Fig. 2 for the standard model. The main reason for the larger apparent thickness is that the condensed sheet, while still thin intrinsically, is more warped. An example of warps is shown in Fig. 13, where the density distribution in a plane perpendicular to the y -axis is plotted; superposition of such warps in different parts of the sheet along the line of sight gives rise to the more puffed-up appearance.

Associated with the sharp warp of condensed material in Fig. 13 is a strong distortion of magnetic field lines. Both are likely driven by protostellar outflows, which are the main source of energy that drives the cloud evolution at late times. In particular, outflows ejected at an angle to the large-scale magnetic field can excite large-amplitude Alfvén waves, which perturb the field lines in the halo that thread other parts of the condensed sheet. The large Alfvén speed in the diffuse halo allows different parts of the sheet to communicate with one another quickly, as emphasized recently by Shu et al. (2007) in the context of poloidally magnetized accretion disks. The communication raises the interesting possibility of global, magnetically mediated, oscillations for the condensed material that may have observational implications. This issue warrants a closer examination in the future.

We conclude by stressing that condensations produced by gravitational settling along field lines do not have to appear highly elongated, even when viewed edge-on. They can be further distorted by outflows from stars formed in neighboring condensations or other external perturbations that are not included in our current calculations. We have experimented with simulations that allow active outflows to re-enter the simulation box, and found that

the condensed sheet became more puffed up and, sometimes, even completely disrupted.

4.2. Outflow Feedback

Protostellar outflow plays an important role in our model. It limits the amount of core mass that goes into a forming star and injects energy and momentum back to the cloud. In our standard model, we have assumed that 75% of the outflow momentum is carried away in a bipolar jet (of 30° in half opening angle), and the remaining 25% in a spherical component. Here, we contrast the standard model with one that has a stronger spherical component (carrying 75% of outflow momentum). The star formation efficiencies (SFEs) of both models are plotted in Fig. 14. It is clear that the stronger spherical component of outflow has reduced the rate (and efficiency) of star formation significantly, by a factor of ~ 2.3 . This trend is the opposite of what we found in the case of cluster formation in dense clumps that are globally magnetically supercritical (Nakamura & Li 2007): for a given total outflow momentum, more spherical outflows tend to drive turbulence on a smaller scale that dissipates more quickly, leading to a higher rate of star formation.

There are a couple of reasons for the seemingly contradictory result. First, whereas the supercritical cluster-forming clumps are supported mainly by turbulent motions, the bulk of the star-forming condensations in subcritical or nearly critical clouds are magnetically supported (in the cross-field direction). As a result, faster dissipation of turbulence leads to more rapid star formation in the former, but not necessarily in the latter. Second, the jet component, while crucial for supporting the more massive, rounder cluster-forming clump, has a more limited effect on the flattened condensation: it escapes easily from the sheet (and quickly out of the simulation box) and its energy is mostly “wasted” as far as driving turbulence in the star-forming, condensed material is concerned. The spherical component, in contrast, impacts the condensed material more directly, especially in the vicinity of a newly formed star. The dispersal of the residual core material after star formation to a wider region appears to be the main reason for the lower star formation rate in the case of stronger spherical component: it takes longer for the more widely dispersed material to recondense and form stars. The stars in the stronger spherical component model are less clustered than those in the standard model, consistent with the above interpretation.

5. Dense Cores

5.1. Identification

A variant of the CLUMPFIND algorithm of Williams et al. (1994) is used for core identification. We apply their “friends-of-friends” algorithm to the density data cube in regions above a threshold density, $\rho_{\text{th,min}}$, and divide the density distribution between $\rho_{\text{th,min}}$ and $\rho_{\text{th,max}}$ into 15 bins equally spaced logarithmically. The maximum is set to $\rho_{\text{th,max}} = 10^3 \rho_0$, the density above which a star (Lagrangian particle) is created if the core mass exceeds the local Jeans mass. The minimum is set to $\rho_{\text{th,min}} = 50 \rho_0$, corresponding to $n_{\text{H}_2} = 1.25 \times 10^4 \text{ cm}^{-3}$ for the fiducial value of initial density. We include only those “spatially-resolved” cores containing more than 30 cells in the analysis, to ensure that their properties are determined with reasonable accuracy. The minimum core mass is thus $M_{\text{c,min}} \equiv \rho_{\text{th,min}} \times 30 \Delta x \Delta y \Delta z = 7.19 \times 10^{-2} M_{J,s}$, where $M_{J,s} \equiv \rho_s L_s^3 \simeq 2.5 M_\odot (T/10\text{K})^{3/2} (n_{\text{H}_2,0}/250 \text{ cm}^{-3})^{-1/2}$ is the Jeans mass of the Spitzer sheet.

In our standard simulation, the cloud material settles into a large scale gas sheet by the time $t \sim 6 t_s$. Soon after, a dense core collapses in a run-away fashion to form the first star, signaling the beginning of active star formation. We will limit our analysis of dense cores to this star-forming phase, which complements the analyses of, e.g., Gammie et al. (2003) and Tilley & Pudritz (2007), which focus on the phase prior to the runaway collapse.

There are typically a handful of dense cores in our standard model at any given time (see Fig. 3), which is too small for a statistical analysis. To enlarge the core sample, we rerun the standard model with a different realization of the initial turbulent velocity field, and include all “resolved” cores at six selected times $t = 6.0, 7.0, 8.0, 9.0, 10.0$, and $11.0 t_s$ from both runs. The total number of cores is 72. Since the majority of them do not survive for more than $1 t_s$ (they do last for several local free-fall times typically), there is relatively little overlap in dense cores from one time to another. We treat all cores independently regardless whether they appear at more than one selected time or not. They have densities in the range $10^4 \sim 10^5 \text{ cm}^{-3}$ and radii of $0.04 \sim 0.12 \text{ pc}$, corresponding roughly to H^{13}CO^+ or N_2H^+ cores.

5.2. Core Shape

We compute the shape of a core using the eigenvalues of the moment-of-inertia tensor:

$$I_{ij} \equiv \int \rho x_i x_j dV , \quad (20)$$

where the components of position vector, x_i and x_j , are measured relative to the center of mass. We compute the lengths of the three principal axes, a, b , and c ($a \geq b \geq c$) by dividing the eigenvalues of the tensor, $M_c a^2$, $M_c b^2$, and $M_c c^2$, by the core mass M_c . The core shape is then characterized by the axis ratios $\xi \equiv b/a$ and $\eta \equiv c/a$.

Figure 15 shows the distribution of axis ratios of the dense cores in our sample. It is clear that the cores are generally triaxial; they show little clustering around either the prolate ($b/a = c/a < 1$) or oblate ($b/a = 1, c < 1$) line in the figure. This result is perhaps to be expected, since the cores are distorted by external turbulent flows and occasionally outflows, neither of which are symmetric. Following Gammie et al. (2003), we divide the ξ - η plane into three parts: a prolate group which lies above the line connecting $(\xi, \eta) = (1.0, 1.0)$ and $(0.33, 0.0)$, an oblate group which lies below the line connecting $(\xi, \eta) = (1.0, 1.0)$ and $(0.67, 0.0)$, and a triaxial group which is everything else. Of the 72 identified cores, 43% (31) are prolate, 44% (32) are triaxial, and 13% (9) are oblate. These fractions are in general agreement with Gammie et al. (2003). One difference is that the ratio $\eta = c/a$ tends to be smaller for our cores [see Figure 10 of Gammie et al. (2003)]. It is likely because dense cores in our model are embedded in a condensed sheet, which has already settled gravitationally along the field lines, although part of the difference may also come from the different methods used in core identification. Note that more massive cores tend to be more flattened along their shortest axis. This trend lends support to the idea that gravitational squeezing plays a role in core flattening.

Another trend is that more massive cores tend to be more oblate. For example, 9 out of 15 (60%) cores having masses more than 1.5 times the average core mass ($\langle M_c \rangle = 0.93 M_{J,s}$) lie below the line connecting $(\xi, \eta) = (1.0, 1.0)$ and $(0.5, 0.0)$ (the dotted line in Fig. 15). Less massive cores tend to be more prolate. Their shapes may be more susceptible to external influences, such as ambient flows.

5.3. Virial Analysis

Virial theorem is useful for analyzing the dynamical states of dense cores. We follow Tilley & Pudritz (2007) and adopt the virial equation in Eulerian coordinates (McKee & Zweibel 1992):

$$\frac{1}{2}\ddot{I} + \frac{1}{2} \int_S \rho r^2 \mathbf{v} \cdot d\mathbf{S} = U + K + W + S + M + F, \quad (21)$$

where

$$I = \int_V \rho r^2 dV, U = 3 \int_V P dV, K = \int_V \rho v^2 dV, W = - \int_V \rho \mathbf{r} \cdot \nabla \Psi dV,$$

$$S = - \int_S [P\mathbf{r} + \mathbf{r} \cdot (\rho\mathbf{v}\mathbf{v})] \cdot d\mathbf{S} , M = \frac{1}{4\pi} \int_V B^2 dV , F = \int_S \mathbf{r} \cdot \mathbf{T}_M \cdot d\mathbf{S} .$$

Here, \mathbf{T}_M is the Maxwell stress-energy tensor

$$\mathbf{T}_M = \frac{1}{4\pi} \left(\mathbf{B}\mathbf{B} - \frac{1}{2}B^2\mathbf{I} \right) , \quad (22)$$

where \mathbf{I} is the unit tensor. The terms, I , U , K , W , S , M , and F denote, respectively, the moment of inertia, internal thermal energy, internal kinetic energy, gravitational energy, the sum of the thermal surface pressure and dynamical surface pressure, internal magnetic energy, and the magnetic surface pressure. The internal thermal, kinetic, and magnetic energies are always positive. The gravitational term is negative for all the cores in our sample, although it can in principle be positive, especially in crowded environments. Other terms can be either positive or negative. The second term on the left hand side of equation (21) denotes the time derivative of the flux of moment of inertia through the boundary of the core. As is the standard practice (e.g., Tilley & Pudritz 2007), we ignore the left hand side of equation (21) in our discussion, and consider a core to be in virial equilibrium if the sum $U + K + W + S + M + F = 0$.

The equilibrium line is shown in Fig. 16, where the sum of the surface terms ($S + F$) is plotted against the gravitational term (W), both normalized to the sum of the internal terms ($U + K + M$). The surface terms (dominated by the external kinetic term) are generally important; they are more so for lower mass cores than higher mass cores. The majority of the cores more massive than 1.5 times the average core mass lie below the equilibrium line, and are thus bound; they are expected to collapse and form stars. The majority of lower mass cores lie, in contrast, above the line, and may disperse away, if they do not gain more mass through accretion and/or merging with other cores, or further reduce their turbulence support through dissipation and/or magnetic support through ambipolar diffusion.

Tilley & Pudritz (2007) found in their ideal MHD simulations that as the mean magnetic field becomes stronger, the surface terms contribute more to the virial equation. Indeed, for their most strongly magnetized cloud, a good fraction of cores have surface terms that are greater than the sum of the internal terms ($U + K + M$). This is not the case for our non-ideal MHD model, even though our clouds are more strongly magnetized than theirs. The reason is that the cloud dynamics is modified by ambipolar diffusion, especially in dense cores, where the diffusion rate is the highest. A related difference is that there are more bound cores in our models than in their strong field models, where most of the cores are magnetically subcritical (see also Dib et al. 2007). Ambipolar diffusion enables these cores to become supercritical, and thus more strongly bound. It is a crucial ingredient that cannot be ignored for core formation, even for relatively weakly magnetized clouds (of dimensionless

mass-to-flux ratio λ of a few). For such clouds, the cores tend to be more strongly magnetized (relative to their masses) than the cloud as a whole, especially in driven turbulence (Dib et al/ 2007), since only a fraction of the cloud mass along any given flux tube is compressed into a core.

The boundedness of a core is often estimated using the virial parameter, the ratio of the virial mass to core mass, particularly in observational studies. In Figure 17, we plot against core mass the virial parameter, defined as

$$\alpha_{\text{vir}} = \frac{5\Delta V_{1D}^2 R_c}{GM_c}, \quad (23)$$

where ΔV_{1D} is the one-dimensional velocity dispersion including the contribution from thermal motion. There is a clear trend for more massive cores to have smaller virial parameters. Indeed, nearly all cores more massive than 1.5 times the average ($M_c \gtrsim 1.5 \langle M_c \rangle \simeq 1.4 M_{J,s}$) have virial parameters smaller than unity. It is consistent with the fact that most of these cores lie below the line of the virial equilibrium in Fig. 16, indicating that they are bound. The reason for the agreement is that the surface terms are not as significant as the gravitational term for massive cores, and that their magnetic support is greatly reduced by ambipolar diffusion (consistent with the trend for cores with smaller flux-to-mass ratios to have smaller virial parameters, see Fig. 16). The reduction of surface terms makes the internal kinetic energy, which is directly related to the virial parameter, more important. We conclude that the virial parameter can be used to gauge the importance of self-gravity for dense cores formed in strongly magnetized clouds, as long as ambipolar diffusion is treated properly. The virial parameter can be fitted by a power law $\alpha_{\text{vir}} \propto M_c^{-2/3}$, in good agreement with the scaling found by Bertoldi & McKee (1992) for nearby GMCs.

5.4. Velocity Dispersion-Radius Relation

The kinematics of molecular clouds and dense cores embedded in them are probed with molecular lines. Since the pioneering work of Larson (1981), many observational studies have shown that the linewidth of a region correlates with the size of the region. The linewidth-size relation is often approximated by a power law $\Delta V \propto R^{0.5}$. However, this relation may not hold universally, especially on small scales. There are many cases where no clear correlation is found between the two (e.g., Caselli & Myers 1995; Lada et al. 1991; Onishi et al. 2002).

In Fig. 18, we plot the three-dimensional nonthermal velocity dispersion against radius (equivalent to the linewidth-size relation) for the cores in our sample. No correlation is apparent between the two, consistent with the observations of Onishi et al. (2002) for the

dense cores in the Taurus molecular clouds. There is a large scattering in the velocity dispersion-radius plot, especially for cores with small masses. The reason may be that some cores (especially the less massive ones) are not in virial equilibrium and that their formation is strongly influenced by external flows.

5.5. Angular Momentum Distribution

Angular momentum is one of the crucial parameters that determine the characteristics of formed stars or stellar systems. In Fig. 19, we plot the specific angular momenta of the cores against their radii. There is no tight correlation between the specific angular momentum and radius, although there is a slight tendency for more massive cores to have somewhat larger specific angular momenta. For our sample cores, the specific angular momentum ranges from 0.01 to $0.4 c_s L_s$ (where c_s is the isothermal sound speed and L_s the Jeans length of the Spitzer sheet). The distribution peaks around $0.08 c_s L_s$, corresponding to $0.9 \times 10^{21} \text{ cm}^2 \text{ s}^{-1}$ (for the fiducial cloud parameters). For comparison, we superpose in the figure the specific angular momenta of 7 starless N_2H^+ cores deduced by Caselli et al. (2002). They are broadly consistent with our results. The average for the N_2H^+ cores is estimated at $\sim 1.6 \times 10^{21} \text{ cm}^2 \text{ s}^{-1}$, somewhat larger than the peak value of our distribution.

An oft-used quantity for characterizing the rotation of a dense core is the ratio of rotational energy to gravitational energy. For a uniform sphere of density ρ rotating rigidly at an angular speed Ω , it is given by $\beta = \Omega^2 / (4\pi G \rho)$. Even though our cores are not uniform, and do not rotate strictly as a solid body, we have computed the value of β using the average angular speed and mean density. The distribution of β peaks around ~ 0.02 , in good agreement with the average value of 0.018 for the starless N_2H^+ cores of Caselli et al. (2002). It is also consistent with the well-known result that rotation is generally not important as far as core support against self-gravity is concerned (Goodman et al. 1993).

5.6. Flux-to-Mass Ratio

Ambipolar diffusion enables dense cores to be less magnetized relative to their masses. In Fig. 20, we plot the magnetic flux-to-mass ratios of the cores against their column densities. The ratio is normalized to the critical value $2\pi G^{1/2}$, and the column density to that of the initially uniform state, $4\pi\rho_0 L_s$. The magnetic flux-to-mass ratio is approximated as $\Gamma_c \equiv \pi R_c^2 \langle B \rangle / M_c$, where $\langle B \rangle$ is the mean magnetic field strength inside a core (e.g., Dib et al. 2007) and the mean core radius R_c is defined as the radius of a sphere enclosing the

same volume as the core. The column density is calculated from the core mass divided by the area of a circle whose radius is equal to R_c . There is a clear trend for cores with higher column densities to have lower flux-to-mass ratios. Indeed, all cores with masses greater than $1.5 \langle M_c \rangle$ are magnetically supercritical, with flux-to-mass ratios as low as ~ 0.35 , indicating that they have all experienced significant ambipolar diffusion. The weakening of magnetic support may have enabled these cores to condense to a high column density in the first place.

5.7. Core Mass Spectrum

In Figure 21 we plot the mass spectrum for our sample of dense cores. The core mass is normalized to the Jeans mass of the Spitzer sheet, $M_{J,s}$. The lowest mass at $\sim 0.1 M_{J,s}$ corresponds to the minimum core mass determined from the criteria for core identification. There is a prominent break around $1 M_{J,s}$ in the mass spectrum. Above the break, the spectrum can be fitted roughly by a power law $dN/dM \propto M^{-2.5}$, not far from the Salpeter stellar initial mass function. We note that cores above the break contain more than ~ 100 cells; their structures should be reasonably well resolved. The core spectrum flattens below the break, which is also broadly consistent with observations. Similar core spectra are also obtained in the turbulent fragmentation model of core formation that involves much weaker magnetic field and much stronger turbulence (e.g., Padoan & Nordlund 2002). The characteristic mass below which the core mass spectrum flattens apparently coincides with the Jeans mass of the condensed sheet, which may result from magnetically regulated gravitational fragmentation. Caution must be exercised in trying to differentiate various scenarios of core formation, such as the magnetically regulated gravitational fragmentation and the turbulent fragmentation, based on core mass spectrum and, perhaps by extension, stellar mass spectrum. The stellar mass spectrum for the 52 stars formed in the standard model and its close variant are plotted in Fig. 21 for comparison. The stellar mass spectrum also resembles the Salpeter IMF.

6. Discussion

6.1. Magnetically-Regulated Star Formation in Quiescent Condensations

We have simulated star formation in relatively diffuse, mildly magnetically subcritical clouds that are strongly turbulent initially. The decay of initial turbulence leads to gravitational condensation of the diffuse material along field lines into a highly fragmented sheet (see Fig. 22), which produces stars in small groups. The bulk of the condensed material

remains magnetically supported in the cross-field direction, however, with typical motions that are moderately supersonic and approximately magnetosonic. Only a small fraction of the condensed material collapses gravitationally to form stars. The calculations lead us to a picture of slow, inefficient, star formation in a relatively quiescent, large-scale condensation (which can be a filament if the cloud is flattened in a direction perpendicular to the field lines to begin with) that is embedded in a much more turbulent halo of diffuse gas.

The above picture is an unavoidable consequence of the anisotropy intrinsic to the large-scale magnetic support. Before the self-gravity becomes strong enough to overwhelm the magnetic support in the cross-field direction (to initiate widespread star formation), it should be able to condense material along the field lines (where there is no magnetic resistance) first. The condensed material is expected to be relatively quiescent. Its field-aligned velocity component is damped during the condensation process, whereas its cross-field motions are constrained by the field lines. The lateral magnetic support ensures that the bulk of the condensed material is relatively long-lived, allowing more time for the turbulence to dissipate. The dissipation is hastened by the high density in the condensation, which makes it easier for shock formation, because of low Alfvén speed. Indeed, when the condensed layer accumulates enough material for its mass-to-flux ratio to approach the critical value (a condition for widespread star formation), its Alfvén speed drops automatically to a value comparable to the sound speed (NL05, Kudoh et al. 2007). Rapid dissipation of super-magnetosonic motions ensures that the bulk of the condensed material moves at no more than moderately supersonic speeds, as we find here and previously in 2D calculations (NL05). It is in this relatively quiescent environment that most star formation takes place.

The quiescent, star-forming, condensed material is surrounded by a highly turbulent, fluffy halo. The stratification in turbulent speed is a consequence of the stratification in density (Kudoh & Basu 2003): the amplitude of a wave increases as it propagates from high density to low density, and faster motions can survive for longer in the lower density region because of higher Alfvén speed. We believe that this is a generic result independent of the source of turbulence. In our particular simulations, the saturated, highly supersonic turbulence in the halo at late times is driven mainly by protostellar outflows internally. It is conceivable, perhaps even likely, that most of the turbulence in the diffuse regions of star forming clouds comes from energy cascade from larger-scale molecular gas (perhaps even HI envelope). Depending on the details of energy injection, the external driving of turbulence can slow down the gravitational settling along field lines and may even suppress it altogether. Even when the large-scale gravitational settling is suppressed, star formation can still occur, perhaps in a less coherent fashion: stars can form in localized pockets of a magnetically subcritical cloud directly from strong compression through shock-enhanced ambipolar diffusion (NL05), especially when the shock is highly super-Alfvénic (Kudoh &

Basu 2008). Vigorous driving may favor a mode of turbulence-accelerated star formation at isolated locations, whereas decay of turbulence may allow the gravity to pull the diffuse gas into large-scale condensations, in which stars form in a more coherent fashion. The first mode is now under investigation, and the results will be reported elsewhere. The second corresponds to the picture outlined above.

The dichotomy is not unique to star formation in strongly magnetized clouds. It is also present when the magnetic field is weak or non-existent: whereas stars form rapidly in a clustered mode in a decaying non-magnetic turbulence, they are produced more slowly, in a more dispersed fashion, if the turbulence is driven constantly, especially on small scales (e.g., Mac Low & Klessen 2004). Different modes of star formation may operate in different environments, and there is a urgent need for sorting out which mode dominates in which environment. In the next subsection, we will concentrate on the Taurus molecular clouds, the prototype of distributed low-mass star forming regions (see Kenyon et al. 2008 for a recent review), and the Pipe nebula, which appears to be a younger version of the Taurus complex (Lada et al. 2008).

6.2. Connection to Observations

6.2.1. *The Taurus Molecular Cloud Complex*

The Taurus molecular cloud complex may represent the best case for the picture of magnetically regulated star formation investigated in this paper. One line of evidence supporting this assertion comes from the studies of young stars by Palla & Stahler (2002). They inferred, using pre-main sequence tracks, that the star formation in the complex has two phases. It began at least 10 Myrs ago, at a relatively low level and in widely dispersed locations (Phase I hereafter). In the last three million years or so, stars are produced at a much higher rate (Phase II). The majority of the stars produced in Phase II are confined within the dense, striated, C¹⁸O filaments (Onishi et al. 2002). Palla & Stahler interpret these results to mean that the Taurus clouds evolved from an initial, relatively diffuse, state quasi-statically. They envision that, during the early epoch of quasi-static contraction, few places have contracted to the point of forming dense cores and protostars, and hence only scattered star formation activity is seen at isolated locations (Phase I). Eventually, further contraction of the cloud leads to the formation of nearly contiguous, dense filaments where multiple cores can form and collapse simultaneously, leading to elevated star formation (Phase II). In view of the discussion in the last subsection, it is natural to identify Phase I with the shock-accelerated mode of star formation in a magnetically subcritical or nearly critical cloud (or sub-region), when the turbulence is still strong enough to prevent large-scale gravitational condensation

along the field lines. In this picture, Phase II started when the turbulence had decayed to a low enough level that the gravity was able to collect enough mass along the field lines into condensed structures for a faster, more organized, mode of star formation to take over.

A salient feature of our picture is that the rate of star formation in Phase II should remain well below the limiting free-fall rate of the condensed material. There is strong evidence that the conversion of dense material in the Taurus clouds into stars is indeed slow. The dense, filamentary material is well traced by C^{18}O , which Onishi et al. (1996) has studied in great detail. These authors estimated a mass and average density for the C^{18}O gas of $M_{\text{C}^{18}\text{O}} \sim 2900 M_{\odot}$ and $n_{\text{H}_2} \sim 4000 \text{ cm}^{-3}$ (comparable to that in the condensed sheet in our simulations). The latter corresponds a free fall time $t_{\text{C}^{18}\text{O},ff} = 4.86 \times 10^5 \text{ yrs}$. The maximum, free-fall, rate of turning C^{18}O material into stars is therefore $\dot{M}_{*,\text{C}^{18}\text{O},ff} \sim 6 \times 10^{-3} M_{\odot} \text{ yr}^{-1}$. This rate is to be compared with the actual rate of star formation in the complex, $\dot{M}_* \sim 5 \times 10^{-5} M_{\odot} \text{ yr}^{-1}$, estimated by Goldsmith et al. (2008) based on an assumed average mass of $0.6 M_{\odot}$ for the 230 stars observed in their mapped region (Kenyon et al. 2008) and a duration of 3 Myrs for Phase II of star formation where most stars are produced (Palla & Stahler 2002). Therefore, the rate of converting the even dense (relative to the diffuse ^{12}CO gas) C^{18}O material into stars is extremely slow, amounting to $\sim 1\%$ per local free fall time. This rate is comparable to those obtained in our simulations.

One may argue that the slow rate of star formation in C^{18}O gas is due to turbulence support. However, the C^{18}O gas in the Taurus clouds is observed to be unusually quiescent. Onishi et al. (1996) estimated a mean equivalent line-width (defined as the integrated intensity divided by the peak temperature of the line) of 0.65 km s^{-1} , corresponding to a 3D velocity dispersion of 0.45 km s^{-1} for a Gaussian profile. The velocity dispersion is ~ 2.4 times the sound speed for a gas temperature of 10 K, indicating that the moderately dense gas traced by C^{18}O is not highly supersonic in general. Indeed, the velocity dispersion is quite comparable to that of the condensed sheet material in our standard model at similar densities (see Fig. 7). Nearly 1/3 ($937 M_{\odot}$ out of $2900 M_{\odot}$) of the C^{18}O gas is classified into 40 cores, which have a mean line-width (FWHM) of 0.49 km s^{-1} , comparable to that estimated above for the C^{18}O gas as a whole. Onishi et al. concluded that most of the cores are roughly gravitationally bound, based on their masses, sizes and line-widths. These authors argued that the general alignment of the minor axes of the cores with the overall field direction indicates that the magnetic field plays a role in their formation. We agree with this assessment. The relatively low velocity dispersion of the C^{18}O gas and the morphology of dense cores provide indirect support for the picture of magnetically regulated star formation.

A more direct test of the picture would come from a determination of the mass-to-flux

ratio. For a given field strength B , the critical column density along the field line is

$$\Sigma_{||,c} = 58.7 B_{20} M_{\odot} \text{ pc}^{-2}, \quad (24)$$

corresponding to an $A_V \approx 2.5 B_{20}$, where B_{20} is the field strength in units of $20 \mu\text{G}$. Goldsmith et al. (2008) estimated a total mass of $2.4 \times 10^4 M_{\odot}$ in their mapped area of $28 \text{ pc} \times 21 \text{ pc}$, yielding an average column density of $40.8 M_{\odot} \text{ pc}^{-2}$ along the line of sight. Only $\sim 2/3$ of the surveyed area have detectable ^{12}CO emission in individual spectra, however (their Masks 1 and 2). For these regions, the total mass and area are $1.95 \times 10^4 M_{\odot}$ and $\sim 392 \text{ pc}^2$, yielding a somewhat higher average column density of $49.7 M_{\odot} \text{ pc}^{-2}$ along the line of sight. If the column density along the field lines is comparable to this value, the corresponding critical field strength would be $16.9 \mu\text{G}$, according to equation (24). About half of the mass ($9807 M_{\odot}$) resides in eight “high-density” regions (such as L1495 and Heiles Cloud 2) that together occupy $\sim 31\%$ of the area, with an average line-of-sight column density of $79.5 M_{\odot} \text{ pc}^{-2}$. This value would correspond to a critical field strength of $27.1 \mu\text{G}$ if the magnetic field is exactly along the line of sight. There is, however, evidence for a large-scale magnetic field in the plane of sky in the Taurus cloud complex from the polarization of background star light. Indeed, the velocity anisotropy measured by Heyer et al. (2008) in a relatively diffuse sub-region points to a magnetic field that is mainly in the plane of sky. If this magnetic orientation is correct, and if matter condenses along the field lines into flattened structures, then projection effects may be considerable. Applying a moderate correction factor of $\sqrt{2}$ (corresponding to a viewing angle of 45°) would bring the average field-aligned column density of the “high-density” regions down to $56.2 M_{\odot} \text{ pc}^{-2}$, with a corresponding critical field strength of $19.2 \mu\text{G}$. It is therefore likely that a magnetic field of order $20 \mu\text{G}$ is strong enough to regulate star formation in the Taurus cloud complex.

The magnetic field strength has been measured for three dense cores in Taurus through OH Zeeman measurements using Arecibo telescope (Troland & Crutcher 2008). They are B217-2, TMC-1 and L1544, with a line-of-sight field strength of $B_{\text{los}} \approx 13.5, 9.1, \text{ and } 10.8 \mu\text{G}$ respectively. Although the true orientation of the magnetic field is unknown, a statistically most probable correction factor of 2 would bring the total field strength to $\sim 18.2 - 27.0 \mu\text{G}$. Given that OH samples moderately dense gas approximately as C^{18}O does, and that the field strength changes relatively little at low to moderate densities (see Fig. 9), it is plausible such a field permeates most of the space in the complex. A worry is that such a strong field is not detected in several other cores in the Taurus in the same Arecibo survey. Whether these non-detections can be reconciled with our picture of magnetically regulated star formation through, e.g., unfavorable field orientation, remains to be seen.

Indirect evidence for a relatively strong magnetic field comes from the observation that the magnetic field as traced by the polarization vectors of the background star light is well

ordered over many degrees in the sky, indicating that the magnetic energy is larger than the turbulent energy. If we use conservative estimates for H_2 number density of 10^2 cm^{-3} (see Table 2 of Goldsmith et al. 2008), and turbulent speed of 2 km s^{-1} , we can put a lower limit to the field strength at $\sim 15 \mu\text{G}$. The limit agrees with the value of $\sim 14 \mu\text{G}$ estimated by Heyer et al. (2008) based on comparing the observed velocity anisotropy in a striated, relatively diffuse region with MHD turbulence simulations; they point out that the value is to be increased if the magnetic field has a substantial component along the line of sight. A strong line-of-sight magnetic field of $\sim 20 \mu\text{G}$ or more is deduced by Wolleben & Reich (2004) at the boundaries of molecular clouds a few degrees away from the sub-region studied by Heyer et al. (2008), from modeling the enhanced rotation measures inferred from polarization observations at 21 and 18 cm. Subsequent HI Zeeman observations did not confirm the deduced field strength, however (C. Heiles, priv. comm.).

Although none of the pieces of evidence discussed above is conclusive individually, taken together, they make a reasonably strong case for a global magnetic field of order $\sim 20 \mu\text{G}$ in strength. The existence of such a field may not be too surprising from an evolutionary point of view. It is now established that the cold neutral medium (CNM) of HI gas (likely precursor of Taurus-like molecular clouds) is fairly strongly magnetized in general, with a median field strength of $\sim 6 \mu\text{G}$ (Heiles & Troland 2005). For denser HI clouds, it is not difficult to imagine a somewhat higher field strength. A case in point is the nearby Riegel-Crutcher HI cloud that we mentioned in the introduction. It was mapped recently by McClure-Griffiths et al. (2006) using 21 cm absorption against strong continuum emission towards the Galactic center. They found long strands of cold neutral hydrogen that are remarkably similar to the CO striations in Taurus studied by Heyer et al. (2008): both are aligned with the local magnetic field. For the magnetic energy to dominate the turbulent energy inside the filaments, the field strength must be of order $30 \mu\text{G}$ or larger. This value is consistent with $B_{los} \sim 18 \mu\text{G}$ obtained by Kazes & Crutcher (1986) through Zeeman measurements at a nearby location, if a correction of ~ 2 is applied for projection effects. The physical conditions inside the HI filaments of the Riegel-Crutcher cloud are not dissimilar to those of diffuse CO clouds: number density $n_H \sim 460 \text{ cm}^{-3}$, velocity dispersion $\sigma \sim 3.5 \text{ km s}^{-1}$, and temperature $T \sim 40 \text{ K}$. The main difference is that the column density is $\sim 10^{20} \text{ cm}^{-2}$, which is not sufficient for shielding the CO from photodissociation (van Dishoeck & Black 1988).

The above discussion leads us to the following scenario for cloud evolution and star formation in the Taurus molecular clouds: we envision the cloud complex to have evolved from a turbulent, strongly magnetized, non-self-gravitating HI cloud similar to the Riegel-Crutcher cloud. Once enough material has been accumulated, perhaps by converging flows (Ballesteros-Paredes et al. 1999) or some other means (such as differential turbulence dissipation),

pation, which may lead to a condensation through “cooling flow” along the field lines, e.g., Myers & Lazarian 1998), for CO shielding, it becomes visible as a molecular cloud. Depending on the degree of magnetization, level of inhomogeneity, and strength of turbulence, star formation can start quickly in some pockets (perhaps even during the process of molecular cloud formation), despite of a strong global magnetic field, either because they happen to be less magnetized to begin with or because their magnetic fluxes are force-reduced by shock-enhanced ambipolar diffusion. This corresponds to the low-level, Phase I of star formation deduced by Palla & Stahler (2002). Once enough material has settled along field lines for the mass-to-flux ratio of the condensed material to approach the critical value, the rate of star formation increases drastically. We identify this phase of more organized star formation in condensed structures as the more active, Phase II of star formation deduced by Palla & Stahler (2002). Even during this relatively active phase, the star formation rate is still well below the free-fall rate of the condensed gas, because of magnetic regulation.

The above picture can be contrasted with that of Ballesteros-Paredes et al. (1999) and Hartmann et al. (2001). These authors advocated a picture of rapid cloud formation and star formation for the Taurus-Auriga complex, motivated mainly by a lack of “post-T Tauri stars” older than ~ 5 Myrs in the region; indeed, the majority of stars are younger than ~ 3 Myrs, as mentioned earlier. They argue that it is difficult to understand how star formation can occur simultaneously over a spatial extent of ~ 20 pc (or more) over a timescale as short as a few million years, given that the observed turbulent speed is ~ 2 km s $^{-1}$, corresponding to a crossing time of ~ 10 Myrs (or more), unless the star formation is coordinated by some agent other than the currently observed turbulence. They suggest that this agent is external: a large-scale converging flow with speeds of 5-10 km s $^{-1}$. In our picture, it is the global gravity and a strong, large-scale, internal magnetic field that coordinate the star formation: the strong field suppresses vigorous star formation until enough material has collected along field lines into condensed structures for the gravity to start overwhelm magnetic support in the cross-field directions. The degree to which the star formation is actually synchronized will, of course, depend on how the mass is initially distributed along the field lines and rate of turbulence dissipation and replenishment, neither of which is, unfortunately, well constrained at the present. Indeed, a hybrid scenario may be possible, with the mass accumulation along the field lines sped up by a large-scale converging flow. Nevertheless, we believe that, at least in the particular case of the Taurus molecular cloud complex, for the large amount of dense, relatively quiescent, C 18 O gas to form stars at $\sim 1\%$ of the free-fall rate, magnetic regulation is needed. A similar case can be made for the Pipe Nebula.

6.2.2. Pipe Nebula

Although less well studied than the Taurus cloud complex, the Pipe nebula is an important testing ground for theories of low-mass star formation in relatively diffuse dark clouds. It has $\sim 10^4 M_\odot$ of molecular material as traced by ^{12}CO (Onishi et al. 1999), not much different from the Taurus complex. The higher density gas traced by ^{13}CO and C^{18}O is concentrated in a long filament that spans more than 10 pc, again similar to the Taurus case. The main difference is that there is no evidence for star formation activity except in the most massive core, B59. The lower rate of star formation indicates that the Pipe nebula is at an earlier stage of evolution compared to the Taurus complex, as pointed out by Muench et al. (2007). The relative inactivity is not due to a lack of dense, quiescent material that is a prerequisite of (low-mass) star formation. J. Alves et al. (2007) identified 159 dense cores from extinction maps, many of which are formally gravitationally unstable, with masses above the critical Bonner-Ebert mass (Lada et al. 2008). In the absence of additional support, such cores should collapse and form stars on the free-fall time scale, which is $t_{ff} = 3.7 \times 10^5$ yrs for the inferred median core density $n(\text{H}_2) = 7 \times 10^3 \text{ cm}^{-3}$. This time scale is much shorter than the turbulence crossing time $t_c = L/v \sim 5 \times 10^6$ yrs, over a region of $L \sim 15$ pc, and for a typical turbulent speed of $v \sim 3 \text{ km s}^{-1}$. The mismatch between the turbulent crossing time and star formation time is therefore much more severe than that noted above for the Taurus region.

There are two possible resolutions to the above conundrum. If the dense cores (at least those massive enough to be formally gravitationally unstable) are indeed short-lived objects, with a lifetime of order the average free-fall time ($\sim 3 \times 10^5$ yrs), their formation must be rapid and well coordinated. It is tempting to attribute the coordination to a large-scale converging flow, as Ballesteros-Paredes et al. (1999) and Hartmann et al. (2001) did for the Taurus case. However, to cover a distance of 15 pc (the size of the cloud, which is comparable to the length of the chain of dense cores) in $\sim 3 \times 10^5$ years, the flow needs to converge at a speed of order $\sim 50 \text{ km s}^{-1}$, which is uncomfortably high. A more likely alternative is that the cores live much longer than their free-fall times would indicate. While the longevity is not necessarily a problem for those non-self-gravitating, lower mass cores that can be confined by external pressure, it is problematic for the more massive cores that should have collapsed on the free-fall time scale, unless they are supported by some (so-far invisible) agent in addition to the observed thermal and turbulent pressures. The most likely candidate is a magnetic field. There is some evidence for the existence of an ordered magnetic field that is more or less perpendicular to the long filament that contains the dense cores from stellar polarization observations (F. Alves & Franco 2007; F. Alves et al., in preparation), although much more work is needed, particularly for the diffuse region outside the filament, to firm up or reject this possibility. In any case, it is plausible that the

Pipe nebula represents an earlier stage of the magnetically regulated cloud evolution and star formation than the Taurus clouds: material has started to collect along the field lines into dense, relatively quiescent, structures, but their mass-to-flux ratios are yet to reach the critical value, except perhaps in the most massive core, B59. In this case, the ages of the cores are set by the rate of mass condensation along the field lines, which may depend on the ill-understood process of turbulence replenishment in the diffuse gas, and may be accelerated by large-scale converging flows (Ballesteros et al. 1999; Hartmann et al. 2001).

6.3. Modes of Star Formation in Strongly Magnetized Clouds

Strong magnetic fields tend to resist cloud condensation and star formation. This resistance can be overcome by either turbulence or gravity, leading to two distinct modes of star formation. Which mode dominates depends on the relative importance of gravity and turbulence. When the turbulence is strong enough to prevent gravitational settling along field lines, star formation is still possible. Turbulence can overcome magnetic resistance in localized regions that are compressed by converging flows to high densities; such regions are expected to have large magnetic field gradients and low fractional ionization, both of which enhance the rate of ambipolar diffusion. The turbulence-accelerated ambipolar diffusion enables dense pockets to become self-gravitating and collapse into stars (NL05, Kudoh & Basu 2008), even when the background cloud remains well supported. In this mode, the crucial step of star formation—core formation—is driven by turbulent converging flows but regulated by magnetic fields, with self-gravity playing a secondary role. After a bound core has formed, its further evolution is driven primarily by the self-gravity, but remains regulated by the magnetic field.

The second mode corresponds to a turbulence that is not strong enough to prevent gravitational settling, either because it is weak to begin with or because it has decayed without being adequately replenished. Condensation would occur along field lines, which would lead to further increase in self-gravity and more rapid dissipation of turbulence. In the condensed structure, turbulence becomes less important dynamically, and star formation is driven mainly by gravity in the cross-field direction. The gravitational contraction is resisted primarily by magnetic fields, although protostellar outflows play an important role in dispersing away the dense gas that remains after the formation of individual stars; the dispersal slows down the global star formation. In this mode, the gravity and magnetic fields are of primary importance, with turbulence playing a secondary role.

The above two modes of star formation may be interconnected: it is natural to expect the second to follow the first, as a result of turbulence dissipation. The transition from

one to the other should occur when the mass-to-flux ratios in the condensed structures approach the critical value. It may be possible for the mass-to-flux ratio to stay near the critical value due to outflow feedback: if too much mass is added to the structure so that its mass-to-flux ratio increases well above the critical value, it would form stars at a higher rate, producing more outflows that stop further mass accumulation, similar to the outflow-regulated scenario of cluster formation envisioned in Matzner & McKee (2000). They have shown that regions of outflow-regulated star formation tend to be overstable, oscillating with increasingly large amplitudes. Indeed, the outflows may unbind the condensed structure completely, terminating its star formation quickly. An abrupt termination is implied by the dearth of the well-observed star forming regions in the declining phase of star formation (Palla & Stahler 2000).

If, on the other hand, outflows fail to retard mass accumulation along field lines, the star formation may change over to yet another, more active, mode — cluster formation. The transition is expected to take place when the mass-to-flux ratios of the condensations become substantially greater than the critical value (say by a factor of two), making global (not just local) contraction perpendicular to the field lines possible. The higher rate of star formation should lead to a stronger outflow feedback, which could increase the turbulence to a level that balances the global collapse (e.g., Nakamura & Li 2007; Matzner 2007). In this mode, protostellar outflow-driven turbulence becomes the primary agent that resists the global gravitational collapse, with the magnetic field playing a secondary role.

In summary, we envision three, perhaps sequential, modes of star formation in strongly magnetized clouds, dominated (a) first by turbulence and magnetic fields, (b) then by magnetic fields and gravity, and (c) finally by gravity and turbulence (again). In this sequence, stars form first directly out of turbulent diffuse material in a dispersed fashion, then more coherently in relatively quiescent, condensed structures, and finally as clusters in dense turbulent clumps. The strong turbulence is primordial initially. It is transformed into a protostellar turbulence by outflows in regions of active cluster formation.

7. Summary and Conclusions

We have performed 3D simulations of star formation in turbulent, mildly magnetically subcritical clouds including protostellar outflows and ambipolar diffusion. The simulations are motivated by observations of molecular gas and young stars in the Taurus cloud complex and the realization that cold neutral HI gas, a likely progenitor of molecular gas, is magnetically subcritical in general. They are natural extensions of our previous 2D calculations. The main results are:

1. The decay of turbulence leads to gravitational condensation of material along the field lines. In the ideal MHD limit, the resulting structure closely resembles a smooth Spitzer sheet, as found previously (Krasnopolsky & Gammie 2005). Ambipolar diffusion changes the structure drastically. It creates supercritical material that behaves differently from the subcritical background in a fundamental way: it can be condensed further by self-gravity. As a result, the distributions of mass with respect to volume and column densities are greatly broadened. Indeed, the probability distribution function (PDF) of the (more easily observable) column density can be fitted approximately by a broad, lognormal distribution (see Fig. 5), as is the case for weakly magnetized clouds fragmented by strong turbulence (e.g., Padoan & Nordlund 2002; P. S. Li et al. 2004). It may be difficult to distinguish the turbulent fragmentation in weakly magnetized clouds and the ambipolar diffusion-enabled gravitational fragmentation in strongly magnetized clouds based on mass distribution.

2. The magnetized clouds evolve into a configuration strongly stratified in density at late times, with dense cores embedded in fragmentary condensations which, in turn, are surrounded by a more diffuse halo (see Fig. 22). The condensed material can be significantly warped and may appear thicker than its intrinsic width, even when viewed edge-on, because of superposition of warps along the line of sight. While the diffuse halo is highly turbulent, the condensations are more quiescent, with moderately supersonic velocity dispersions in general. One reason is that the bulk of the condensed material is magnetically supported, which allows more time for the turbulence to decay. Another is their relatively low Alfvén speed (comparable to the sound speed), which forces highly supersonic motions to dissipate quickly, through shock formation. The moderately supersonic turbulence is maintained, however, for many local free-fall times, through a combination of outflow feedback, MHD waves, and gravitational motions induced by ambipolar diffusion.

3. Stars form at a low rate. Only one percent or less of the cloud material is converted into stars in a free-fall time at the characteristic density of the condensed material. The slow star formation cannot be due to support by turbulence because the star-forming, condensed material is rather quiescent. It is regulated by magnetic fields. The low rate of star formation is not sensitive to the level of initial turbulence, although more turbulent clouds produce stars early, consistent with the picture of turbulence-accelerated star formation in strongly magnetized clouds. The rate of star formation is further reduced by protostellar outflow, particularly the component in the plane of mass condensation.

4. Dense cores formed in our simulations are typically triaxial. More massive cores tend to have lower magnetic flux-to-mass ratios, be more tightly bound gravitationally, and be more oblate. Virial analysis indicates that the surface term due to external kinetic motions contributes significantly in general, especially for less massive cores. We find a larger

number of bound cores than in previous ideal MHD simulations even though our clouds are more strongly magnetized; they are made possible by ambipolar diffusion. The cores have specific angular momenta comparable to the observed values, and a mass spectrum that resembles the Salpeter stellar IMF towards the high mass end. The spectrum flattens near the characteristic Jeans mass of the condensed material, which is a few solar masses for typical parameters. The stellar mass spectrum also resembles the Salpeter IMF.

5. The Taurus molecular cloud complex may represent the best case for magnetically regulated star formation. The strongest evidence comes from the existence of a large amount of dense, relatively quiescent, C^{18}O gas, which produces stars at a rate two orders of magnitude below the maximum free-fall rate. Most likely, the star formation is regulated by a strong, ordered magnetic field. Several lines of evidence suggest that a magnetic field of the required strength (of order $\sim 20\mu\text{G}$) is indeed present in the region, although direct Zeeman measurements are available for only three cores, and their interpretations are complicated by projection effects.

6. We speculate that, depending on the (uncertain) rates of turbulence replenishment and outflow feedback, there may be three distinct modes of star formation in strongly magnetized clouds: (a) inefficient star formation through turbulence-accelerated ambipolar diffusion at dispersed locations in relatively diffuse, magnetically subcritical clouds, (b) more coherent, but still inefficient, magnetically regulated star formation in relatively quiescent, nearly magnetically critical condensations, (c) more efficient cluster formation in magnetically supercritical clumps that may be regulated by outflow-driven protostellar turbulence. Much work remains to be done to understand these modes and their possible interconnection.

This work is supported in part by a Grant-in-Aid for Scientific Research of Japan (18540234, 20540228), and NSF and NASA grants (AST-0307368 and NAG5-12102). Parts of this work were performed while the authors were in residence at the Kavli Institute for Theoretical Physics at UCSB. The numerical calculations were carried out mainly on NEC SX8 at YITP in Kyoto University, on Fujitsu VPP5000 at the Center for Computational Astrophysics, CfCA, of the National Astronomical Observatory of Japan, and on Hitachi SR8000 at Center for Computational Science in University of Tsukuba.

REFERENCES

- Alves, F. O. & Franco, G. A. P. 2007, *A&A*, 470, 597
- Alves, J., Lombardi, M. & Lada, C. F. 2007, *A&A*, 462, 17

- Andre, P., Ward-Thompson, D. & Barsony, M. 1993, *ApJ*, 406, 122
- Ballesteros-Paredes, J. Hartmann, L., & Vazquez-Semadeni, E. 1999, *ApJ*, 527, 285
- Basu, S. & Ciolek, G. E., 2004, *ApJ*, 607, 39
- Bertoldi, F. & McKee, C. F. 1992, *ApJ*, 395, 140
- Caselli, P. & Myers, P. C. 1995, *ApJ*, 446, 665
- Dib, S., Vazquez-Semadeni, E., Kim, J., Burkert, A., & Shadmehri, M. 2007, *ApJ*, 661, 262
- Elmegreen, B. G. 2007, *ApJ*, 668, 1064
- Gammie, C. F., Lin, Y.-T., Stone, J. M., & Ostriker, E. C. 2003, *ApJ*, 592, 203
- Goldsmith et al. 2008 (astro-ph/arXiv:0802.2206)
- Gomez, M. Hartmann, L., Kenyon, S. J., & Hewett, R. 1993, *ApJ*, 105, 1927
- Hartmann, L., Ballesteros-Paredes, J. & Bergin, E. A. 2001, *ApJ*, 562, 852
- Heiles, C. & Crutcher, R. M. 2005, in *Cosmic Magnetic Fields, Lecture Notes in Physics*, vol. 664, pp137-182
- Heiles, C. & Troland, T. H. 2005, *ApJ*, 624, 773
- Heyer, M., Gong, H., Ostriker, E. Brunt, C. 2008, (astro-ph/arXiv:0802.2084)
- Heyer, M. H., Frederick, J., Snell, R. L., Schloerb, F. P., Strom, S. E., Goldsmith, P. F., & Strom, K. M. 1987, *ApJ*, 321, 855
- Ikeda, N., Sunada, K., & Kitamura, Y. 2007, *ApJ*, 665, 1194
- Kazes, I. & Crutcher, R. M. 1986, *A&A*, 164, 328
- Kenyon, S. J. & Hartmann, L. 1995, *ApJS*, 101, 117
- Kenyon et al. 2008, to appear in *Handbook of Star Forming Regions*, ASP Conference Series, ed. B. Reipurth
- Krasnopolsky, R. & Gammie, C. F. 2005, *ApJ*, 635, 1126
- Krumholz, M. R. & Tan, J. C. 2007, *ApJ*, 654, 304
- Krumhotz, M. & McKee, C. F. 2005, *ApJ*, 630, 250

- Kudoh, T., Basu, S., Ogata, Y., & Yabe, T. 2007, MNRAS, 380, 499
- Kudoh, T., & Basu, S. 2003, ApJ, 595, 842
- Kudoh, T., & Basu, S. 2006, ApJ, 642, 270
- Lada, E. A., Bally, J., & Stark, A. A., 1991, ApJ, 368, 432
- Lada, C. J., Muench, A. A., Rathborne, J., Alves, J.F., Lombardi, M. 2008, ApJ, 672, 410
- Larson, R. B. 1981, MNRAS, 194, 809
- Li, P. S., Norman, M. L., Mac Low, M.-M. & Heitsch, F. ApJ, 605, 800
- Li, Z.-Y. & Nakamura, F. 2004, ApJ, 609, L83
- Li, Z.-Y. & Nakamura, F. 2006, ApJ, 640, L187
- Mac Low, M.-M., Klessen, R. S., Burkert, A., & Smith, M. D. 1998, Phys. Rev. Lett., 80, 2754
- Matzner, C. D. 2007, ApJ, 659, 1394
- Matzner, C. D. & McKee, C. F. 2000, ApJ, 545, 364
- McClure-Griffiths, N. M., Dickey, J. M., Gaensler, B. M., Green, A. J., & Haverkorn, M. 2006, ApJ, 652, 1339
- McKee, C. F. 1989, ApJ, 345, 782
- McKee, C. F. & Ostriker, E. C. 2007, ARA&A, 45, 565
- McKee, C. F. & Zweibel, E. G. 1992, ApJ, 399, 551
- Mouschovias, T. & Ciolek, G. 1999, in The Origins of Stars and Planetary Systems, ed. C. Lada & N. Kylafis (Kluwer), p. 305
- Muench, A. A. Lada, C. J., Rathborne, J. M. Alves, J. F., & Lombardi, M. 2007, ApJ, 671, 1820
- Myers, P. C. & Lazarian, A. 1998, ApJ, 507, 157
- Nakamura, F. & Li, Z.-Y. 2005, ApJ, 631, 411
- Nakamura, F. & Li, Z.-Y. 2007, ApJ, 662, 395

- Nakamura, F., Matsumoto, T., Hanawa, T. & Tomisaka, K. 1999, *ApJ*, 510, 274
- Nakano, T. 1984, *Fundam. Cosmic. Phys.*, 9, 139
- Nakano, T. & Nakamura, T. 1978, *PASJ*, 30, 681
- Novak, G., Dotson, J. L. & Li, H. 2007, *ApJ*, in print (arXiv:0707.2818)
- Onishi, T., Mizuno, A., Kawamura, A., Ogawa, H. & Fukui, Y. 1996, *ApJ*, 465, 815
- Onishi, T., Mizuno, A., Kawamura, A., Tachihara, K. & Fukui, Y. 2002, *ApJ*, 575, 950
- Ostriker, E. C., Gammie, C. F. & Stone, J. M. 2001, *ApJ*, 546, 980
- Padoan, P. & Nordlund, A. 2002, *ApJ*, 576, 870
- Palla, F. & Stahler, S. W. 2000, *ApJ*, 540, 255
- Palla, F. & Stahler, S. W. 2002, *ApJ*, 581, 1194
- Price, D. & Bate, M. R. 2008, *MNRAS*, in press
- Shu, F. H. 1991, *Physics of Astrophysics, Vol. 2: Gas Dynamics* (Mill Valley: University Science Books)
- Shu, F. H., Adams, F. C., & Lizano, S. 1987, *ARA&A*, 25, 23
- Shu, F. H. & Li, Z.-Y. 1997, *ApJ*, 475, 251
- Shu, F. H., Galli, D., Lizano, S., Glassgold, A. E. & Diamond, P. H. 2007, *ApJ*, 665, 535
- Tamura, M., Nagata, T., Sato, S. & Tanaka, M. 1987, *MNRAS*, 224, 413
- Tilley, D. & Pudritz, R. 2007, *MNRAS*, 382, 73
- Troland & Crutcher 2008 (astro-ph/arXiv:0802.2253v1)
- van Dishoeck, E. F. & Black, J. H. 1988, *ApJ*, 334, 771
- Williams, J. P., de Geus, E. J., & Blitz, L. 1994, *ApJ*, 428, 693
- Wolleben, M. & Reich, W. 2004, *A&A*, 427, 537

Table 1. Model Parameters

Model	\mathcal{M}	η	AD	Note
S0	3	0.75	yes	standard model
S1	3	0.75	yes	different realization of initial velocity field
S2	3	0.25	yes	stronger spherical outflow component
M0	10	0.75	yes	stronger initial turbulence
I0	3	N/A	no	ideal MHD counterpart of standard model

Note. — All models have the same initial distributions of mass and magnetic field. The field strength is given by the dimensionless ratio of magnetic to thermal pressure $\alpha = 24$, corresponding to a mildly magnetically subcritical cloud of flux-to-mass ratio $\Gamma_0 = 1.1$. The models differ in initial turbulent Mach number \mathcal{M} , jet momentum fraction η , random realization of the initial velocity field, and whether ambipolar diffusion (AD) is included or not.

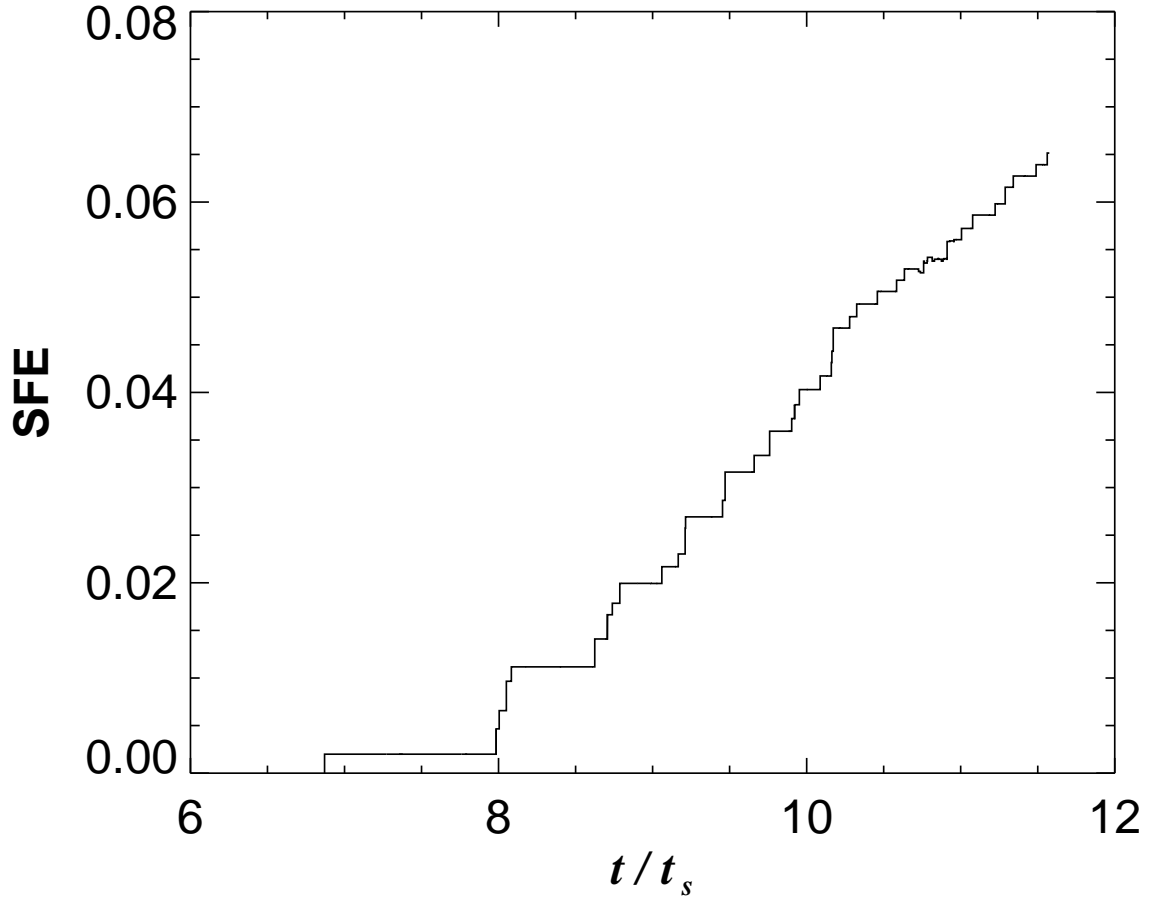


Fig. 1.— Star formation efficiency (SFE) in the standard model as a function of time in units of the collapse time of the condensed sheet t_s . The slope of the curve indicates that less than 1 % of the cloud mass is converted into stars per local free-fall time of the condensed sheet.

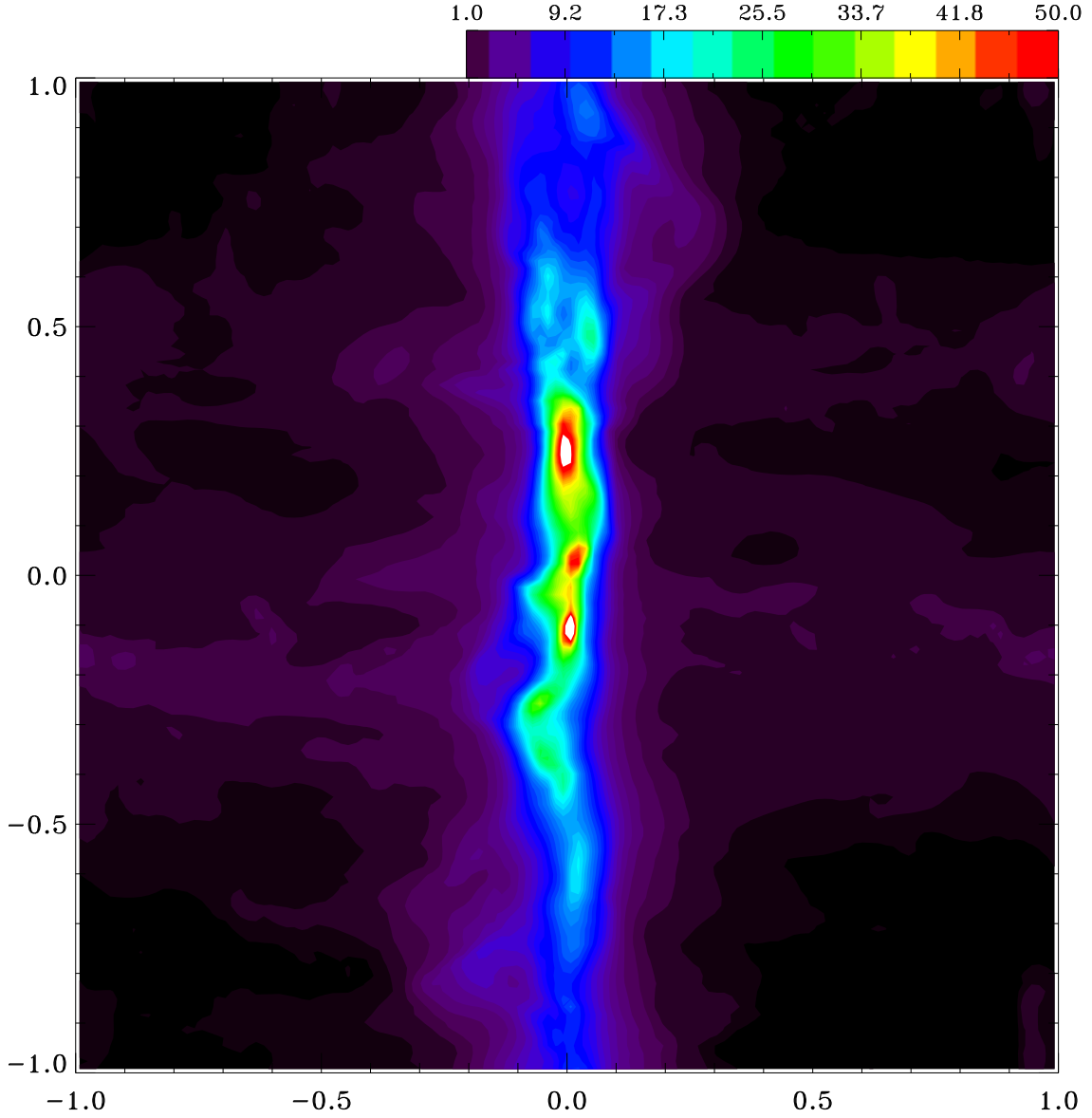


Fig. 2.— An edge-on view of the condensed sheet at a representative time $t = 11 t_s$, showing the column density distribution along the y -axis, which is perpendicular to the direction of initial magnetic field. The condensation is surrounded by a diffuse halo, with some spurs streaking away perpendicular to the sheet. The length is in units of L_J (the Jeans length of the initial uniform state), and column density in the color-bar in units of $\rho_0 L_J$. The three lowest contours have values of 0.05, 0.15, and 0.5, respectively, and are not shown in the color-bar. They are plotted to highlight the structure of the diffuse gas.

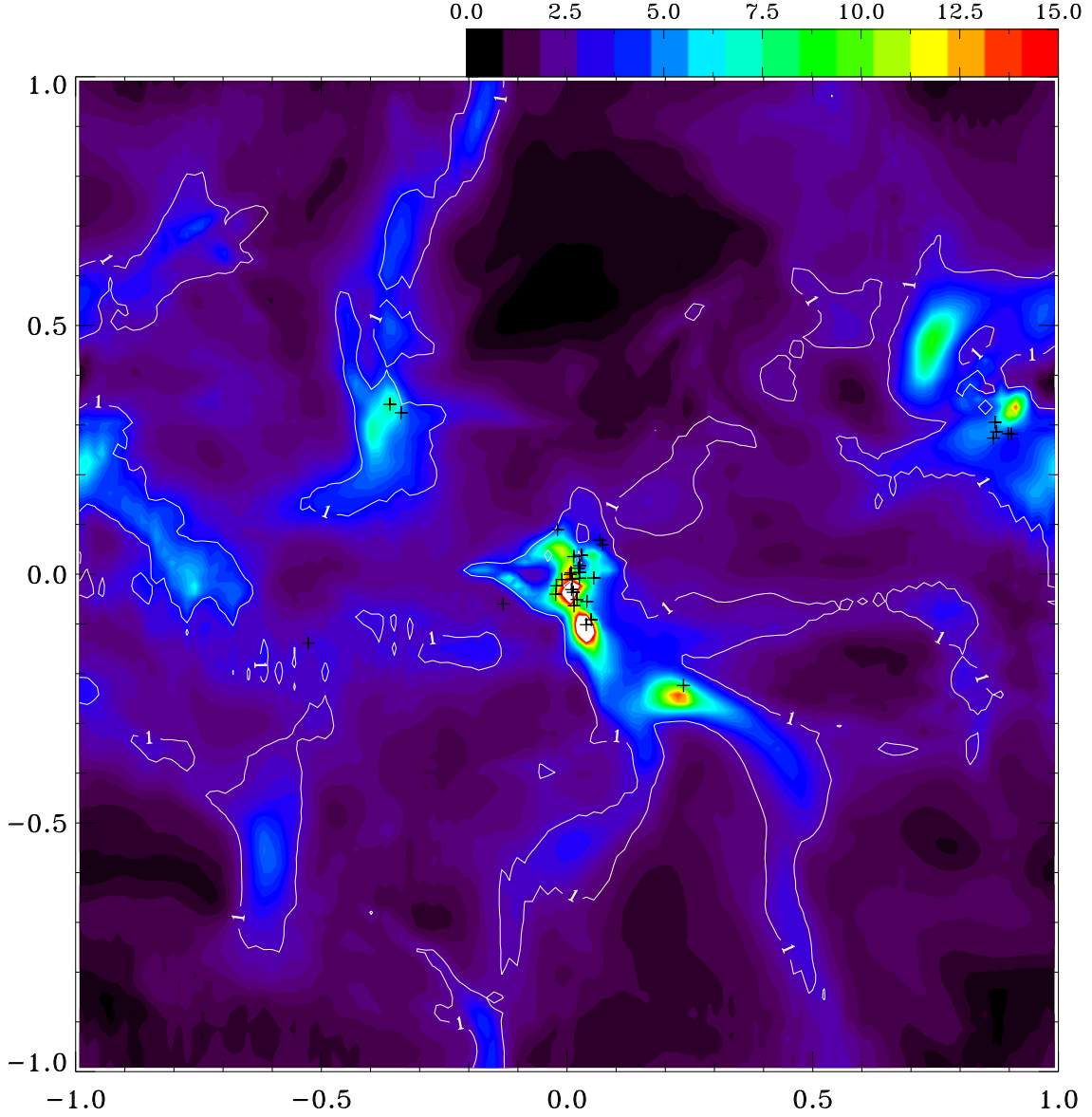


Fig. 3.— Face-on view of the same condensed sheet as in Fig. 2, showing the column density distribution along the x -axis, the direction of initial magnetic field. Superposed are stellar positions (crosses) and contours of critical average mass-to-flux ratio ($\bar{\lambda} = 1$, see equation [19]). The contours divide the magnetically supercritical material capable of star formation from the ambient subcritical material sterile to star formation.

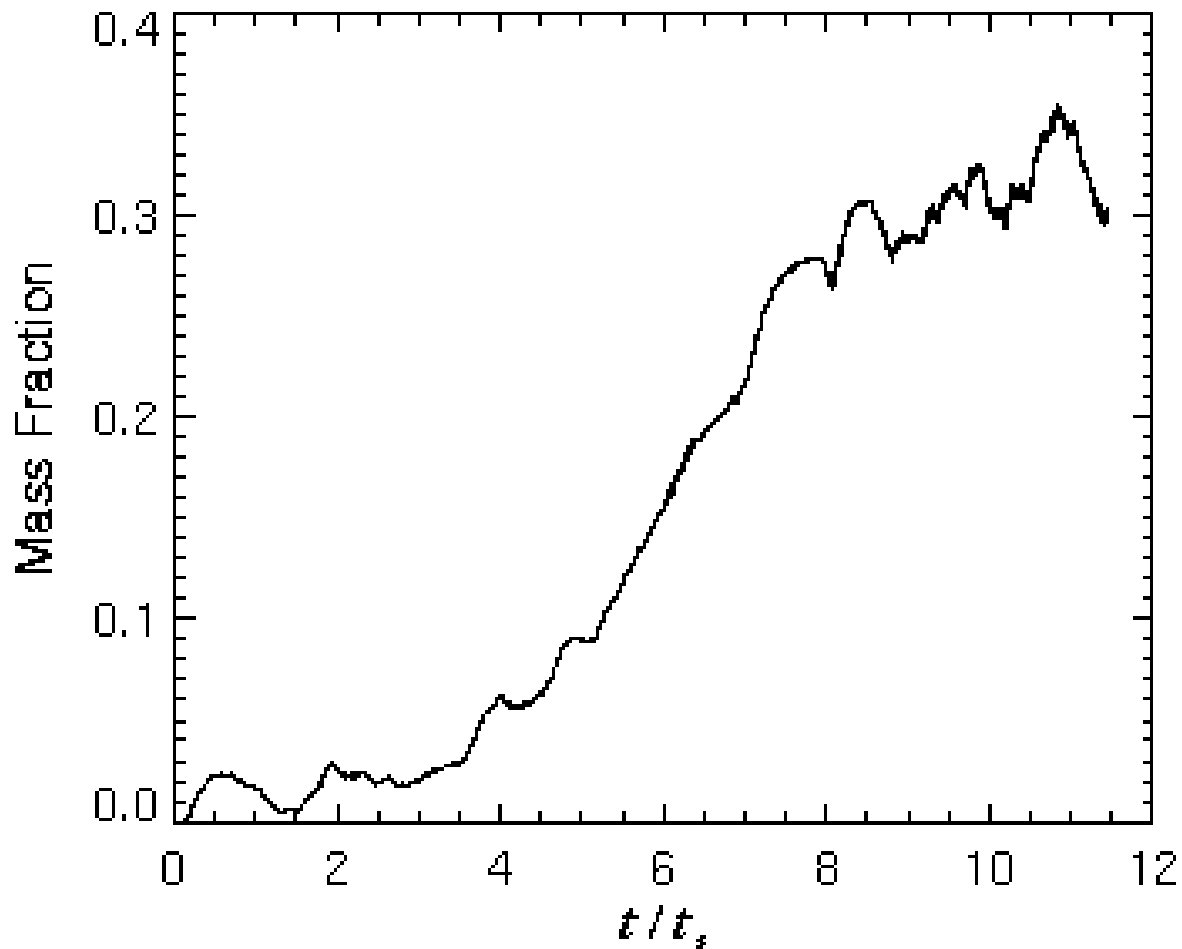


Fig. 4.— Mass fraction of magnetically supercritical material created in the initially subcritical cloud of the standard model through ambipolar diffusion. The mass fraction of supercritical gas increases gradually initially, reaching a plateau at late times.

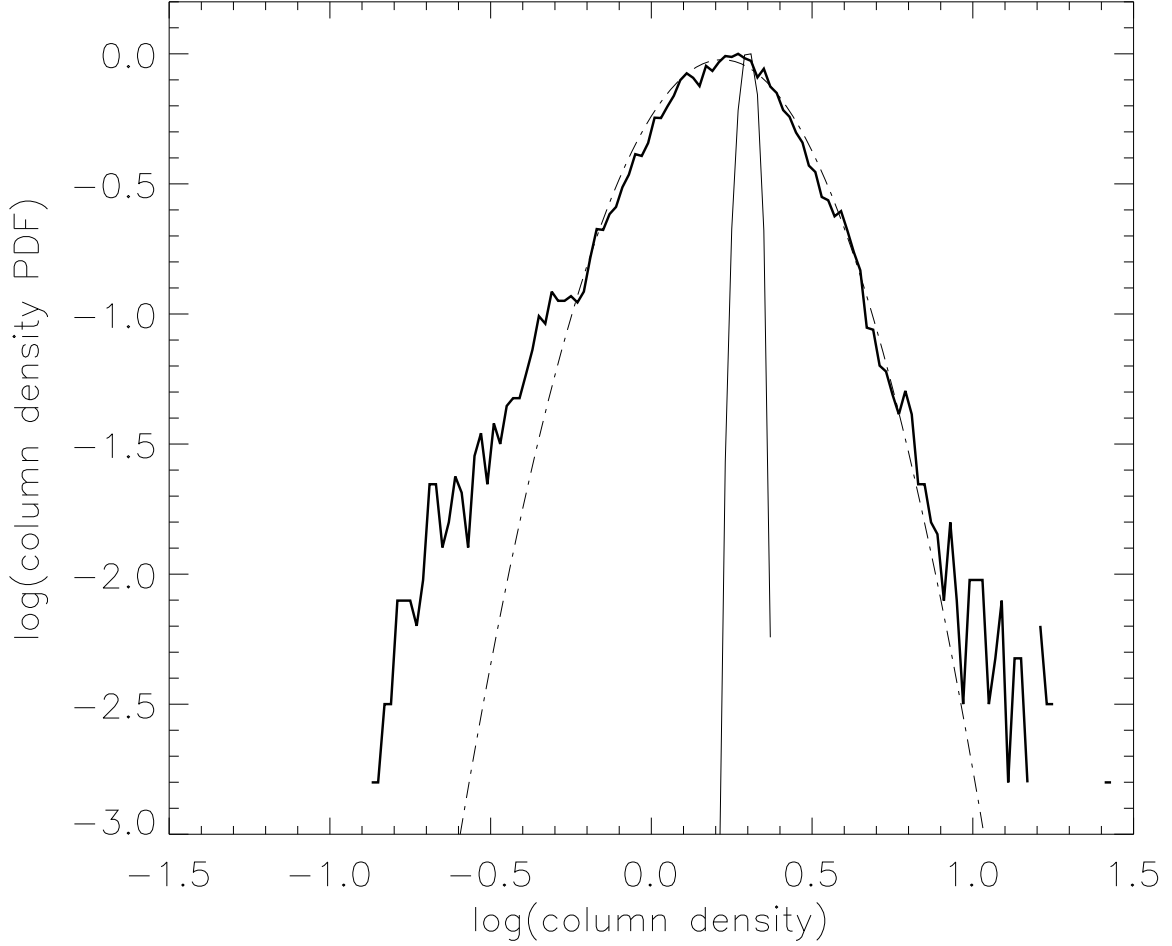


Fig. 5.— The PDF of the face-on column density of the standard model shown in Fig. 3 (*thick solid line*), with a fitted lognormal distribution (*dashed-dotted line*) superposed. The distribution is normalized so that the peak value is close to unity, and the column density is in units of $\rho_0 L_J$. Also plotted for comparison is the column density PDF for the ideal MHD counterpart of the standard model (*thin solid line*), which is much narrower. The stark contrast between the two PDFs highlights the key role of ambipolar diffusion in fragmenting strongly magnetized clouds.

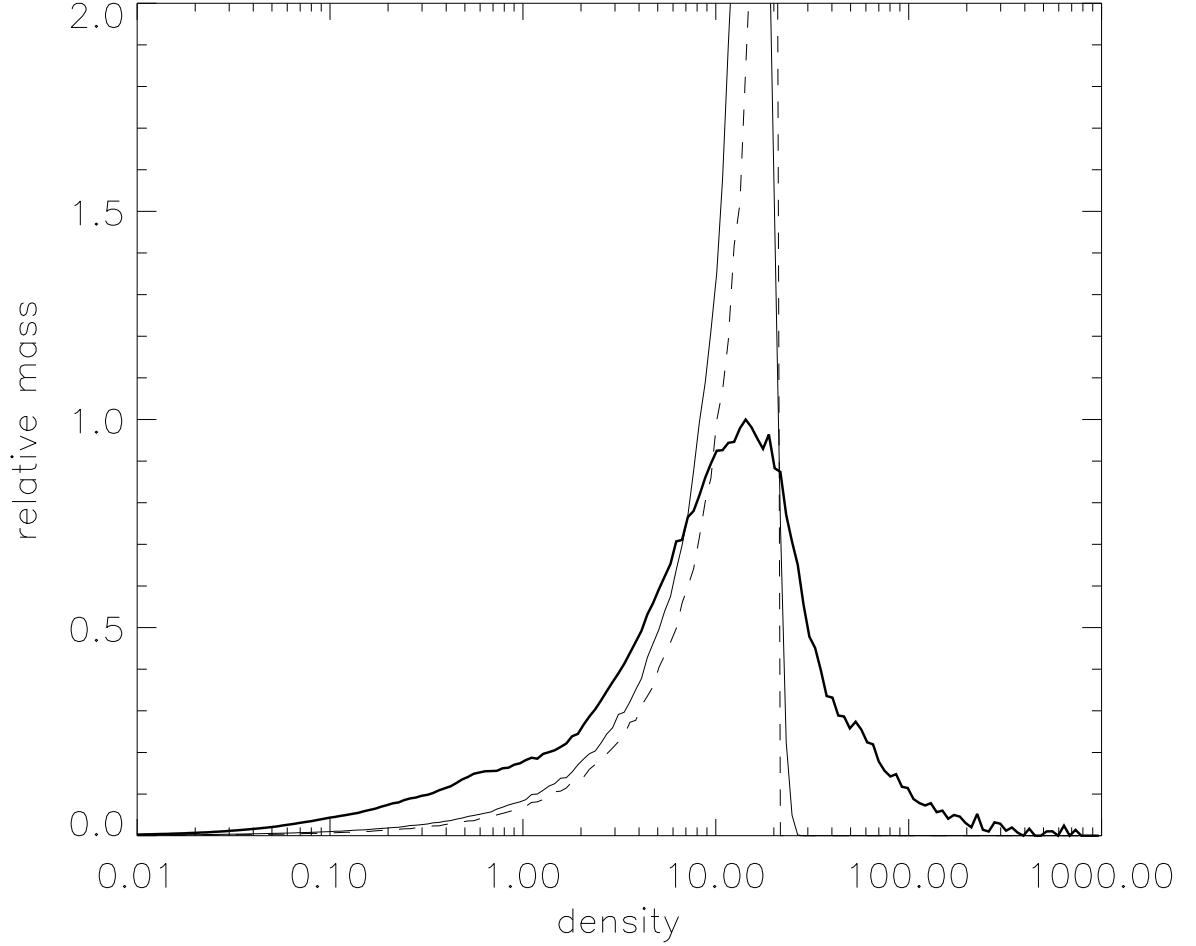


Fig. 6.— Distribution of mass as a function of density (in units of initial density ρ_0 , *thick solid line*), along with that for the ideal MHD case (*thin solid line*) and for a Spitzer sheet containing the same amount of mass (*dashed line*). The mass distribution is much broader in the presence of ambipolar diffusion, because of (magnetically-diluted) gravitational fragmentation.

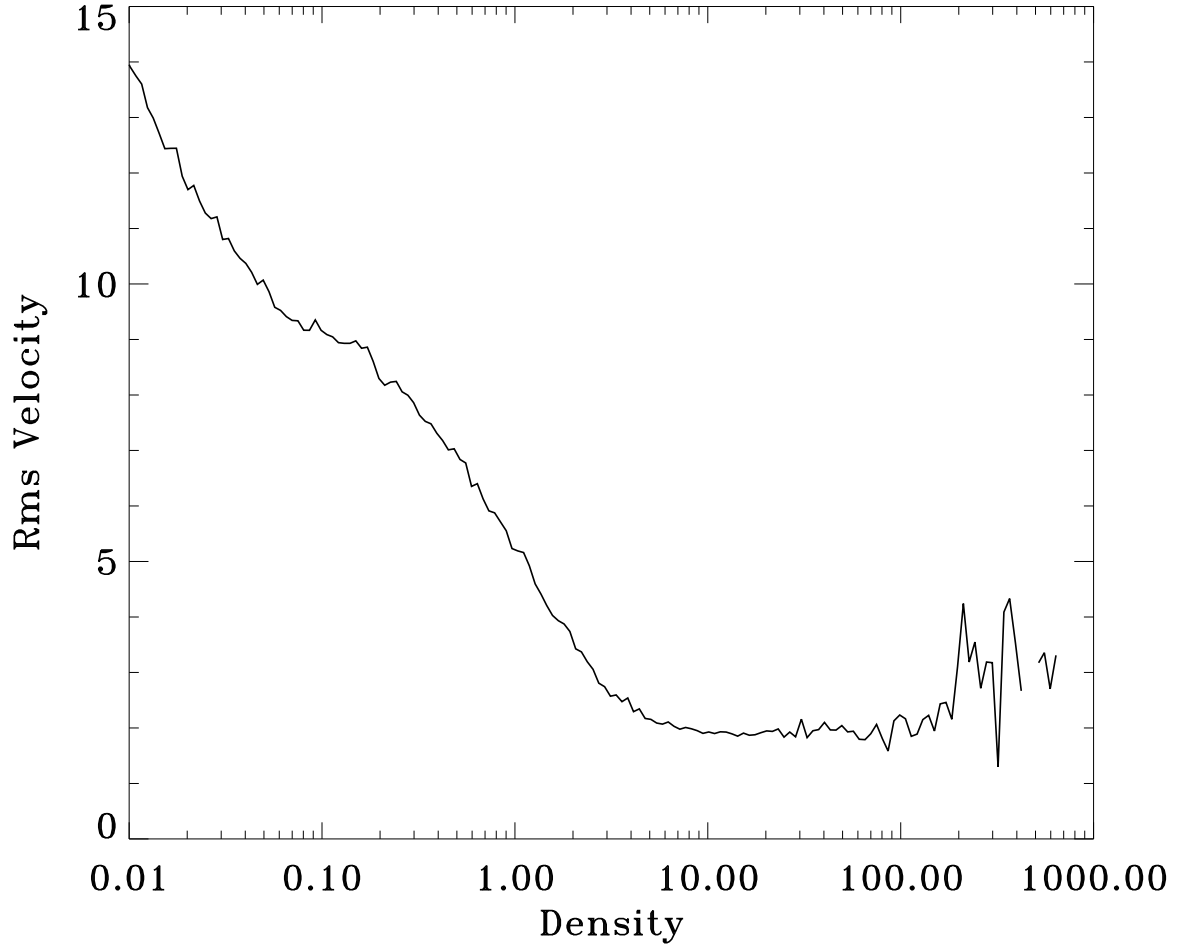


Fig. 7.— Distribution of mass-weighted rms velocity (in units of sound speed c_s) as a function of density (in units of ρ_0), showing that the diffuse halo is much more turbulent than the condensed sheet.

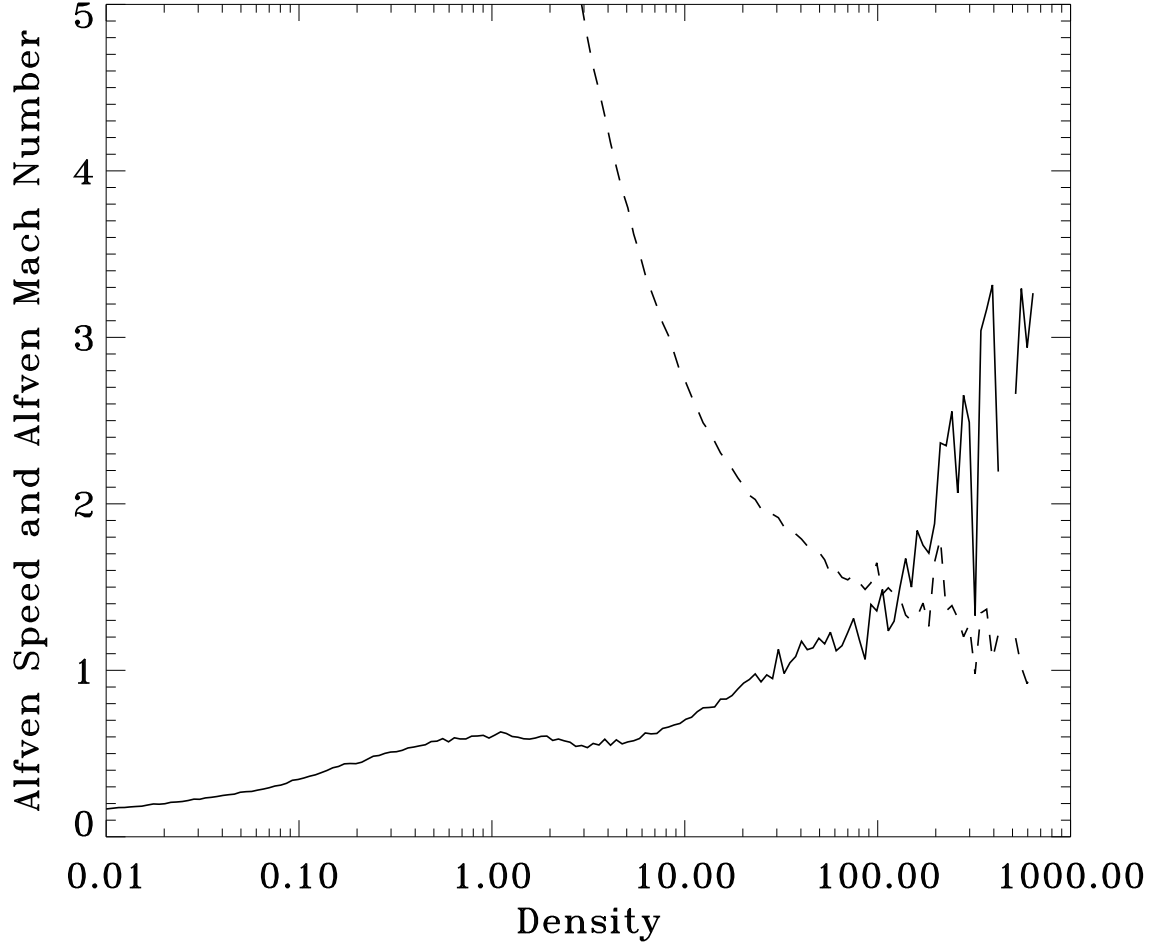


Fig. 8.— Distribution of the average Alfvén Mach number M_A (*solid line*) and Alfvén speed (in units of sound speed, *dashed line*) as a function of density (in units of ρ_0), showing that the motions of the bulk condensed sheet materials are roughly Alfvénic whereas those of the halo materials are sub-Alfvénic.

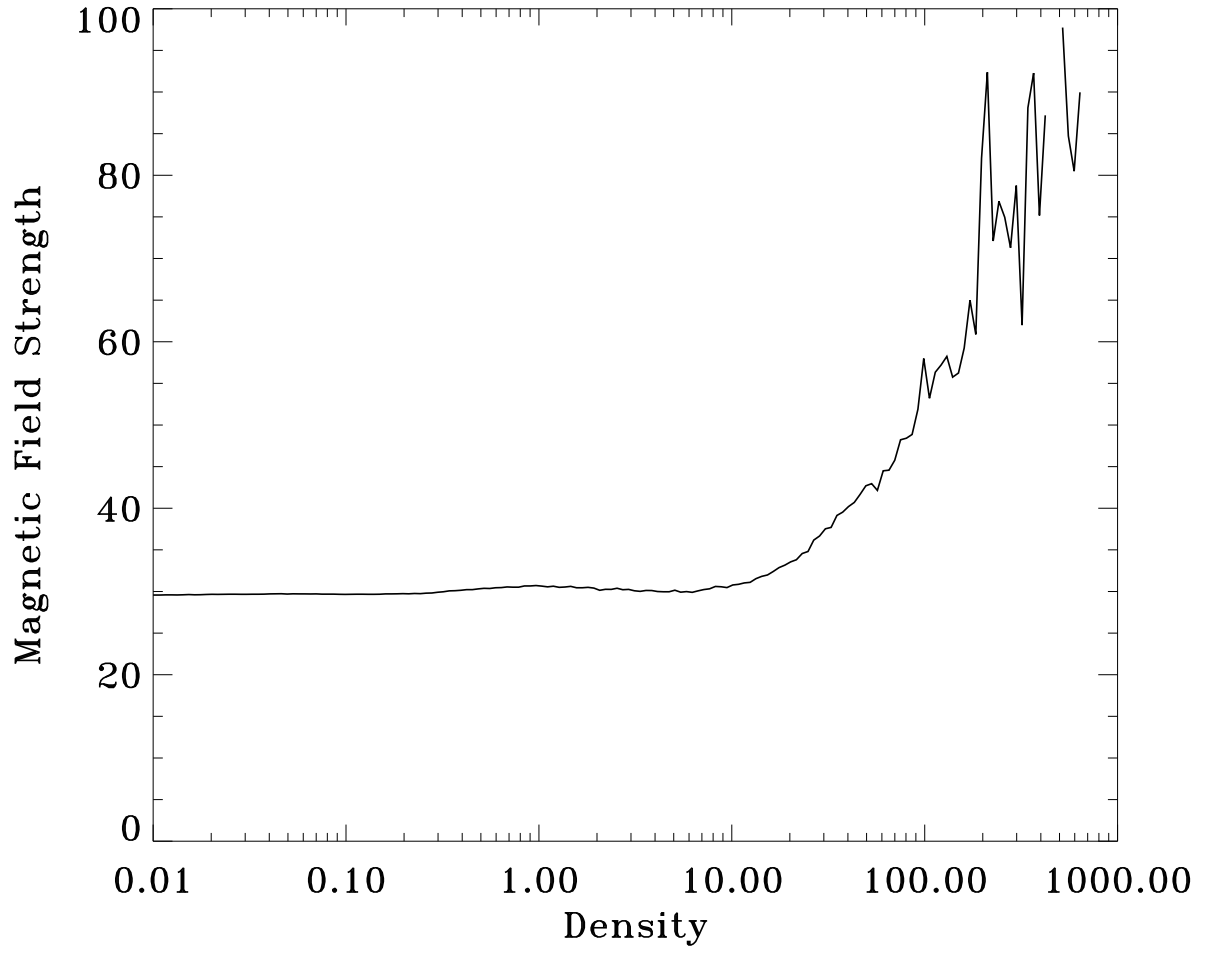


Fig. 9.— Distribution of average magnetic field strength (in units of the initial B_0 , see eq. [12]) as a function of density (in units of ρ_0).

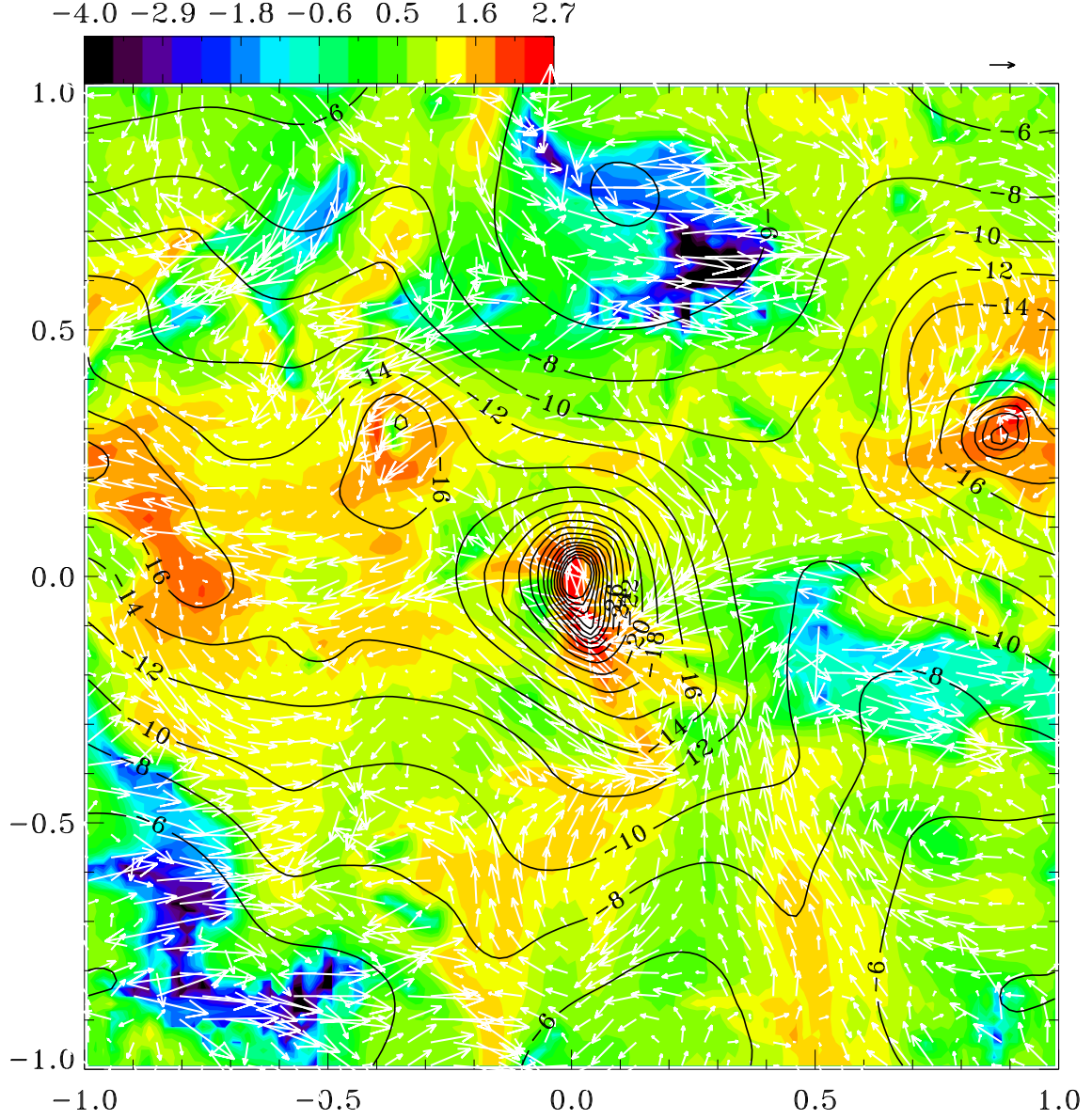


Fig. 10.— Map of the logarithm of the density (in units of ρ_0) in the “midplane” of the condensed sheet. Overlaid are contours of gravitational potential (in units of sound speed squared) and velocity vectors (with a unit vector of length equal to sound speed shown above the panel for comparison).

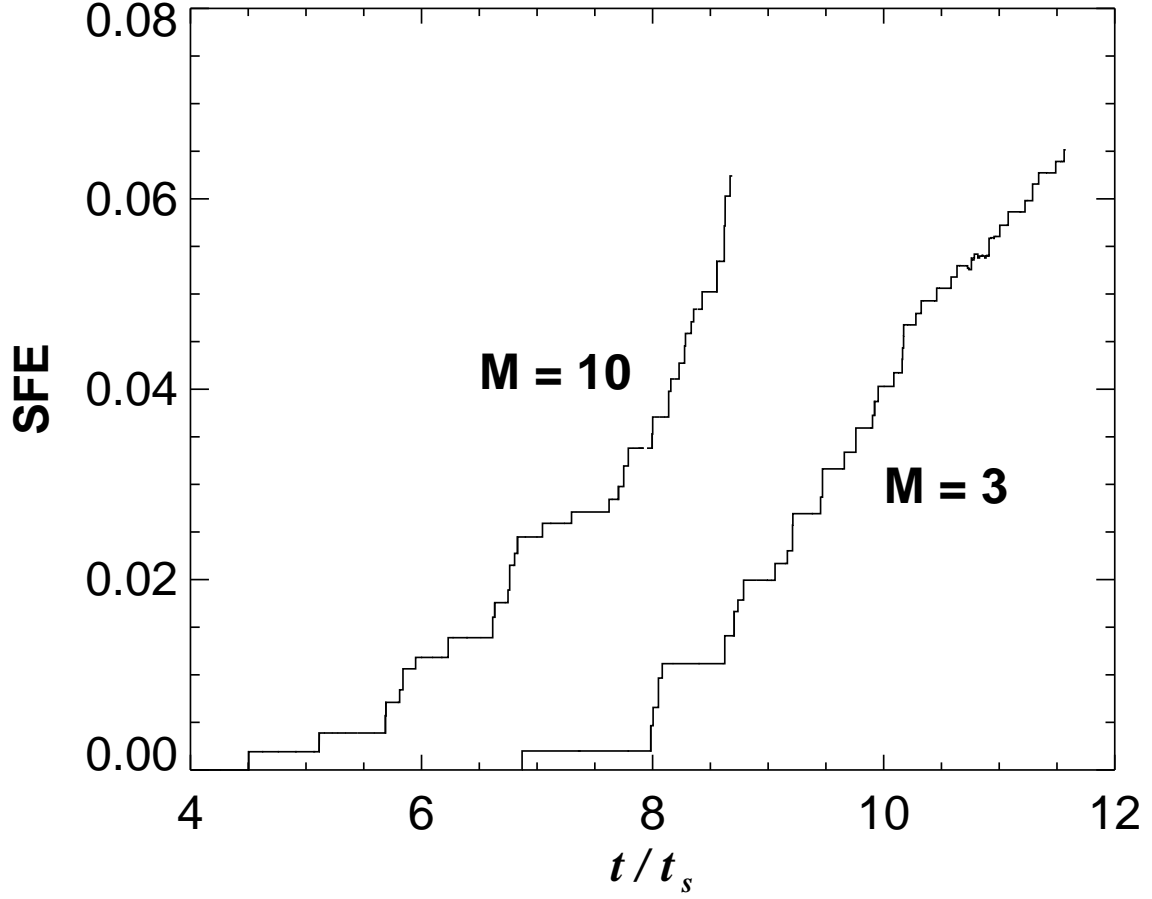


Fig. 11.— Star formation efficiencies as a function of time for two models with initial turbulent Mach number $\mathcal{M} = 10$ and 3 (standard model), respectively. Stars form earlier in the initially more turbulent cloud, illustrating acceleration of star formation by turbulence in strongly magnetized clouds.

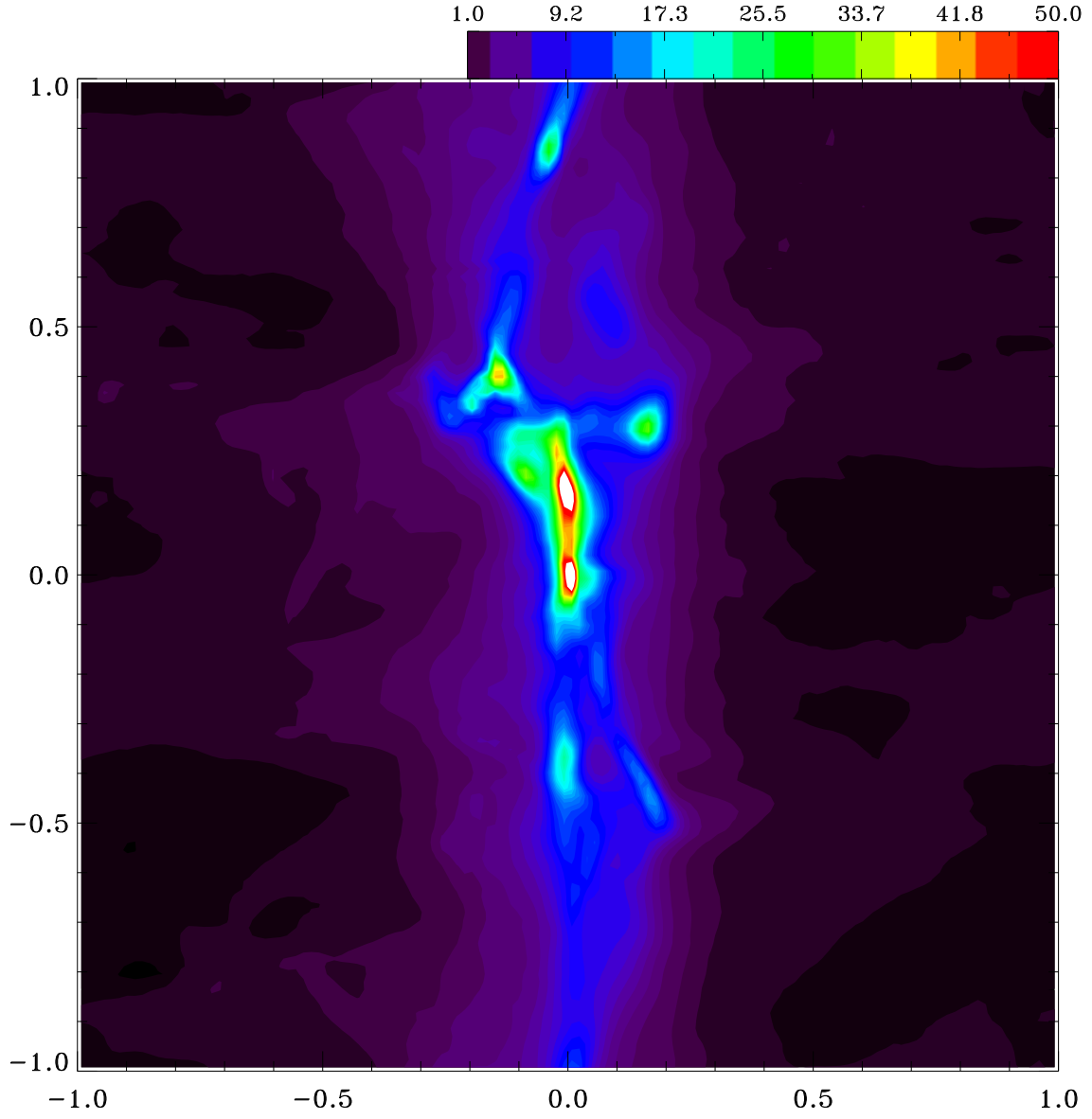


Fig. 12.— Same as Fig. 2 but for an initial turbulent Mach number $\mathcal{M} = 10$, showing that the initially more turbulent model has an apparently thicker condensed sheet than the standard model.

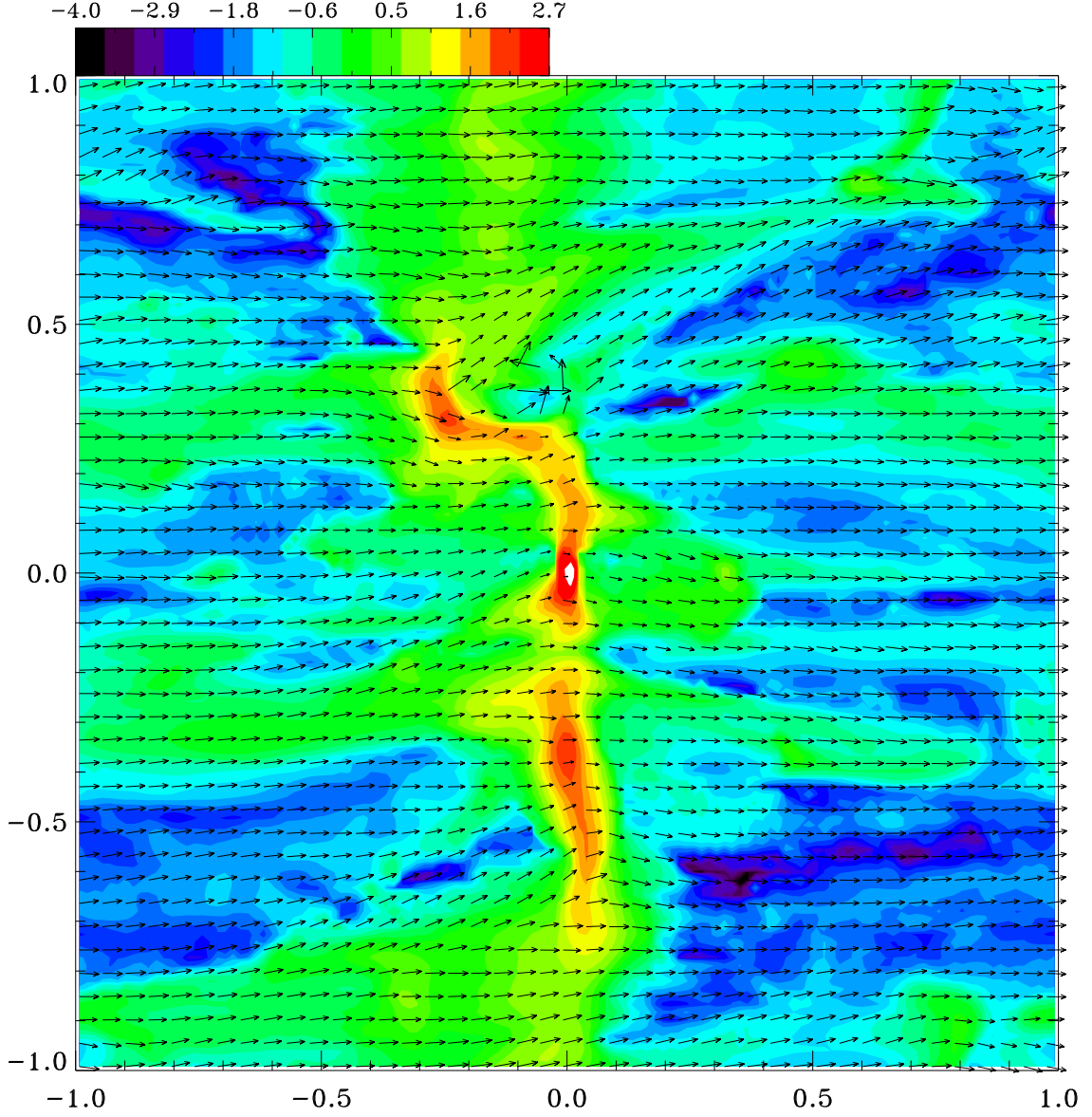


Fig. 13.— Map of the logarithm of the density (in units of ρ_0) in an xz plane that passes through the minimum of gravitational potential. Superposed are unit vectors for magnetic field directions. Note the prominent warp at $z \sim 0.3$. Superposition of such warps along the line of sight can make the condensed sheet appear thicker than its intrinsic thickness, as illustrated in Fig. 12.

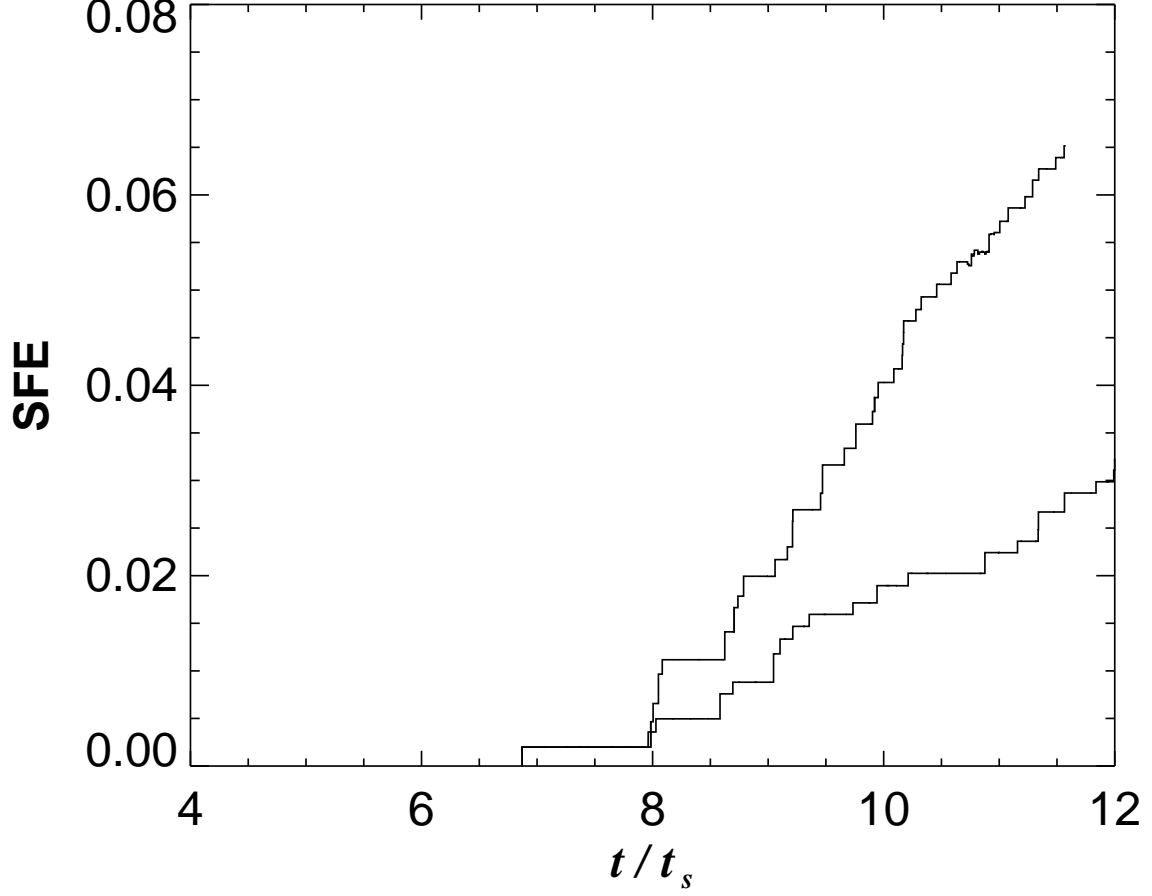


Fig. 14.— Star formation efficiencies as a function of time for two models with outflow momentum dominated by, respectively, the bipolar jet (*upper curve*, standard model) and spherical component (*lower curve*), showing that the spherical component of outflow is more efficient in slowing down star formation in flattened condensations of strongly magnetized clouds.

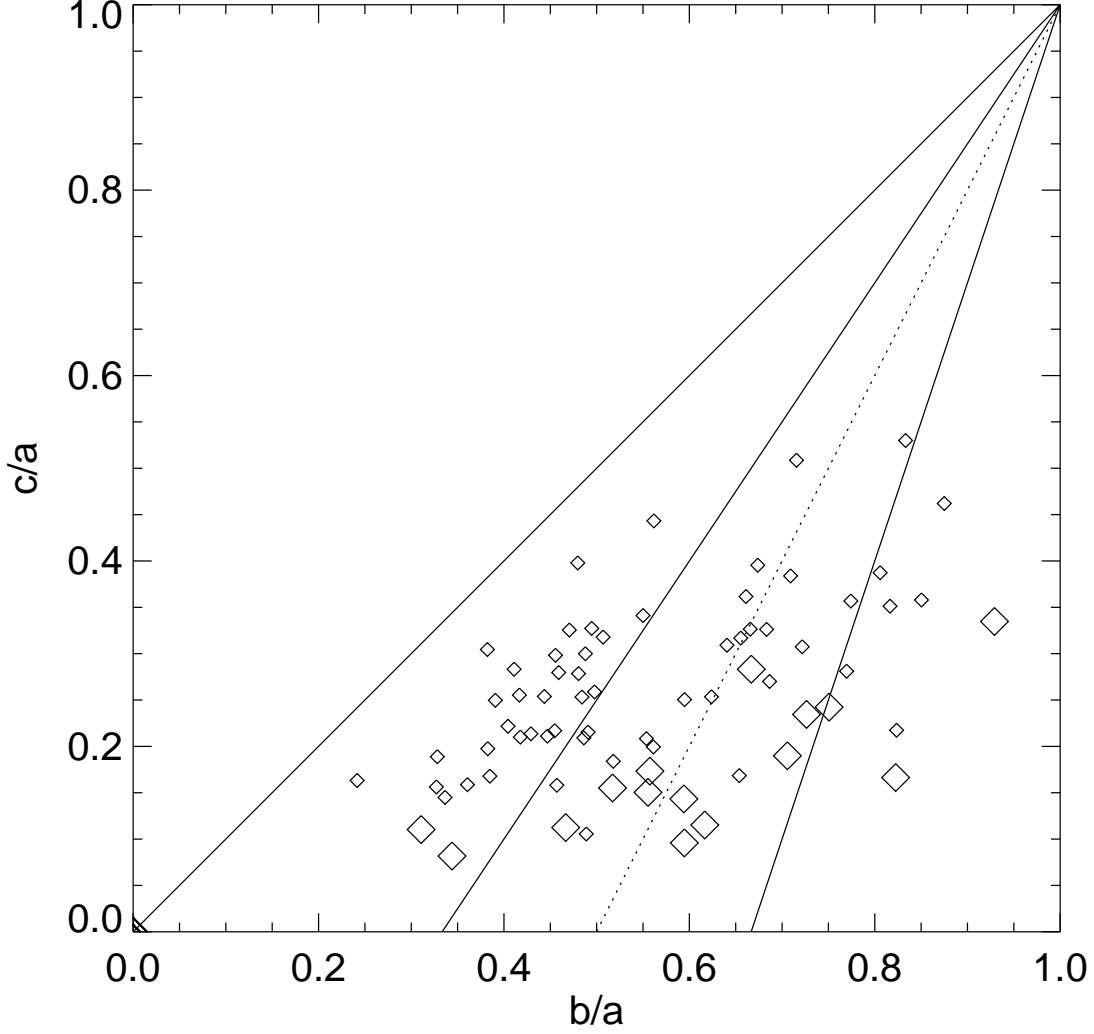


Fig. 15.— Distribution of axis ratios of dense cores formed after the first star was created. The abscissa and ordinate are the axis ratios of $\xi = b/a$ and $\eta = c/a$, respectively. A large symbol indicates a core with a mass greater than $1.5 \langle M_c \rangle$, while a small symbol indicates a core with a smaller mass. We divide the ξ - η plane into three parts: a prolate group which lies above the line connecting $(\xi, \eta) = (1.0, 1.0)$ and $(0.33, 0.0)$, an oblate group which lies below the line connecting $(\xi, \eta) = (1.0, 1.0)$ and $(0.67, 0.0)$, and a triaxial group which is everything else. For comparison we draw the dotted line that connects $(\xi, \eta) = (1.0, 1.0)$ and $(0.5, 0.0)$.

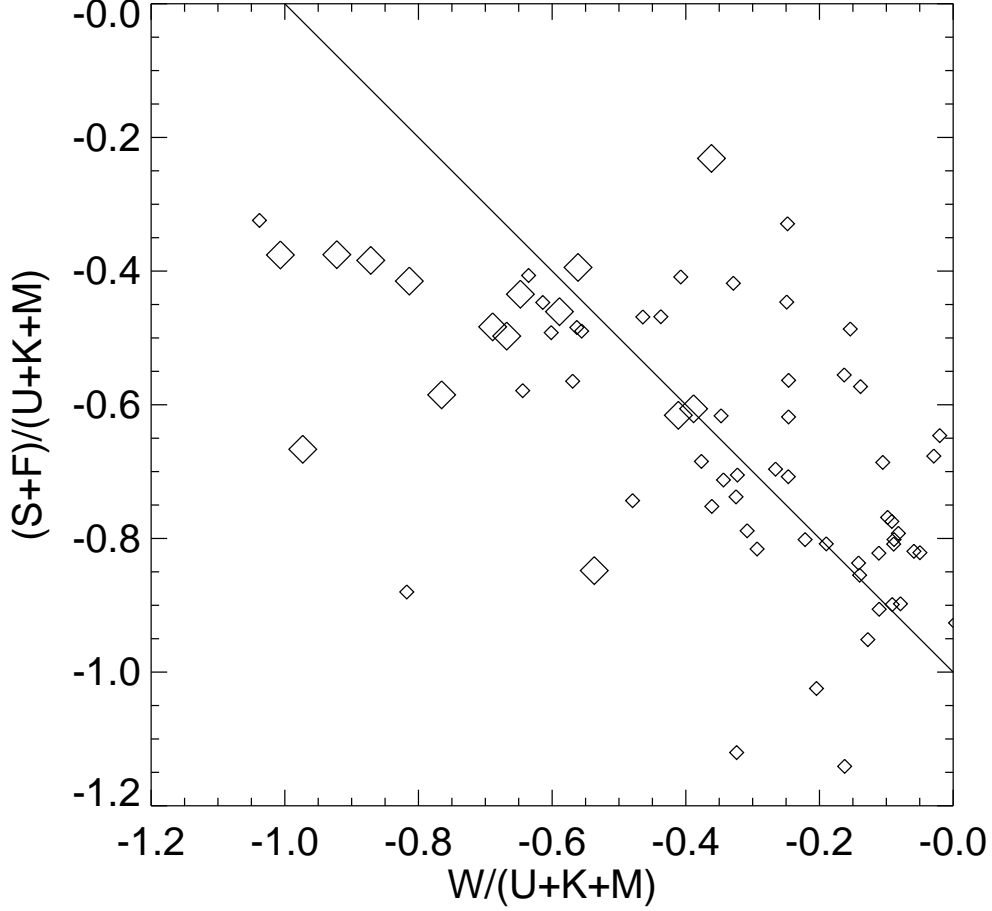


Fig. 16.— The relationship between the sum of the two surface terms, $S + F$, and the gravitational term, W , in the virial equation. They are normalized to the sum of the internal terms, $U + K + M$. The solid line indicates the virial equilibrium, $U + K + W + S + M + F = 0$. The large and small symbols are the same as those of Figure 15. For the cores that lie below the line, the left hand side of the virial equation (21) is negative and thus expected to be bound. All others that lie above the line are unbound and expected to disperse away, if they do not gain more mass through accretion and/or merging with other cores, or reduce internal support through turbulence dissipation and/or magnetic flux reduction through ambipolar diffusion.

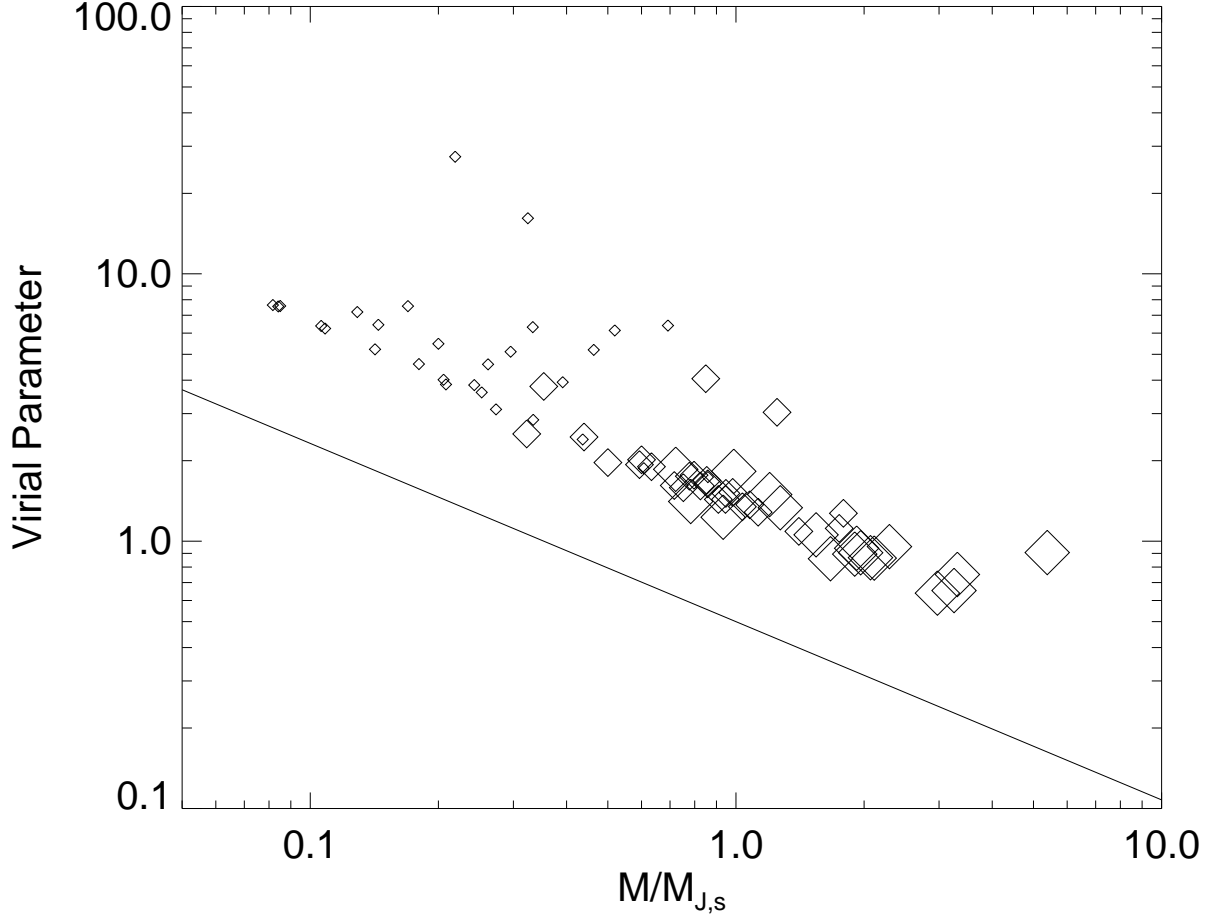


Fig. 17.— The virial parameter as a function of the core mass. Large, intermediate, and small symbols denote, respectively, cores with $\Gamma_c \leq 0.5$, $0.5 < \Gamma_c \leq 0.7$, and $\Gamma_c > 0.7$, where Γ_c is the flux-to-mass ratio of a core. The virial parameter can be fitted by a power law of $\alpha_{\text{vir}} \propto M_c^{-2/3}$, indicated by the solid line.

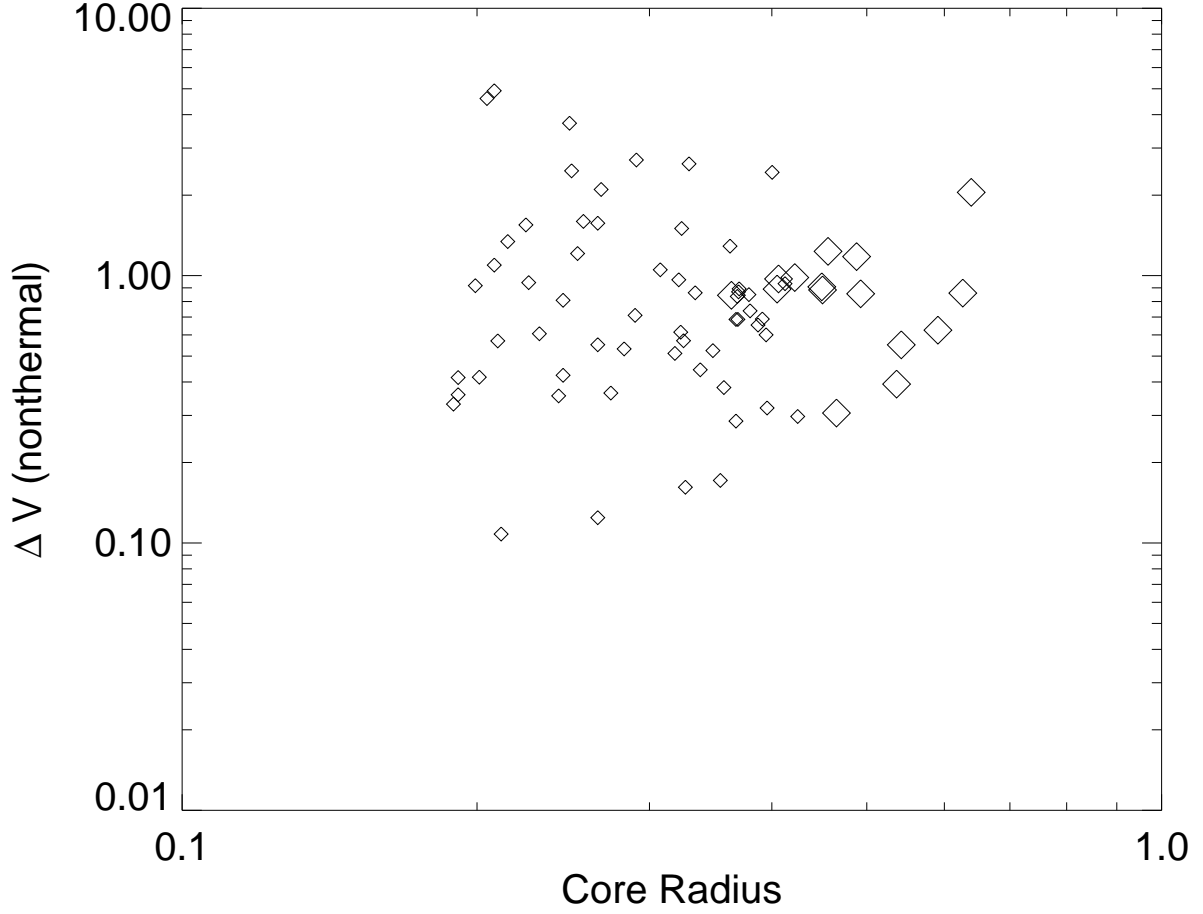


Fig. 18.— The nonthermal velocity dispersion as a function of core radius. The velocity dispersion is normalized to the sound speed c_s , and radius to the Jeans length of the Spitzer sheet L_s . The large and small symbols are the same as those of Figure 15. There is apparently no correlation between the velocity dispersion and the radius, in good agreement with the observed linewidth-size relation of the dense cores in the Taurus molecular clouds (Onishi et al. 2002).

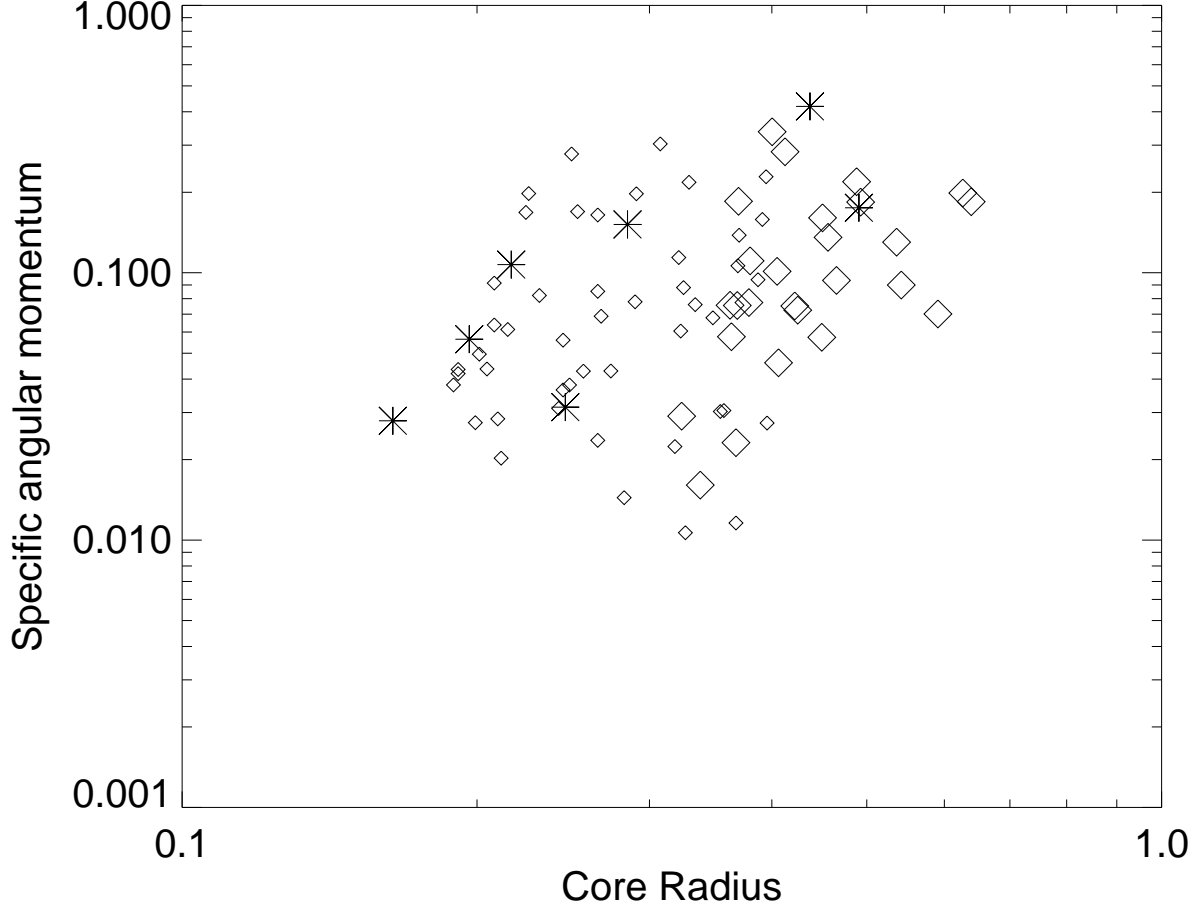


Fig. 19.— Distribution of specific angular momentum as a function of core radius. The specific angular momentum is normalized to $c_s L_s = 1.1 \times 10^{22} \text{ cm}^2 \text{ s}^{-1}$ (for our fiducial cloud parameters), and radius to the Jeans length of the Spitzer sheet L_s . The large and small symbols are the same as those of Figure 15. For comparison, the specific angular momenta of 7 starless N_2H^+ cores are plotted as asterisks (data from Table 5 of Caselli et al. 2002).

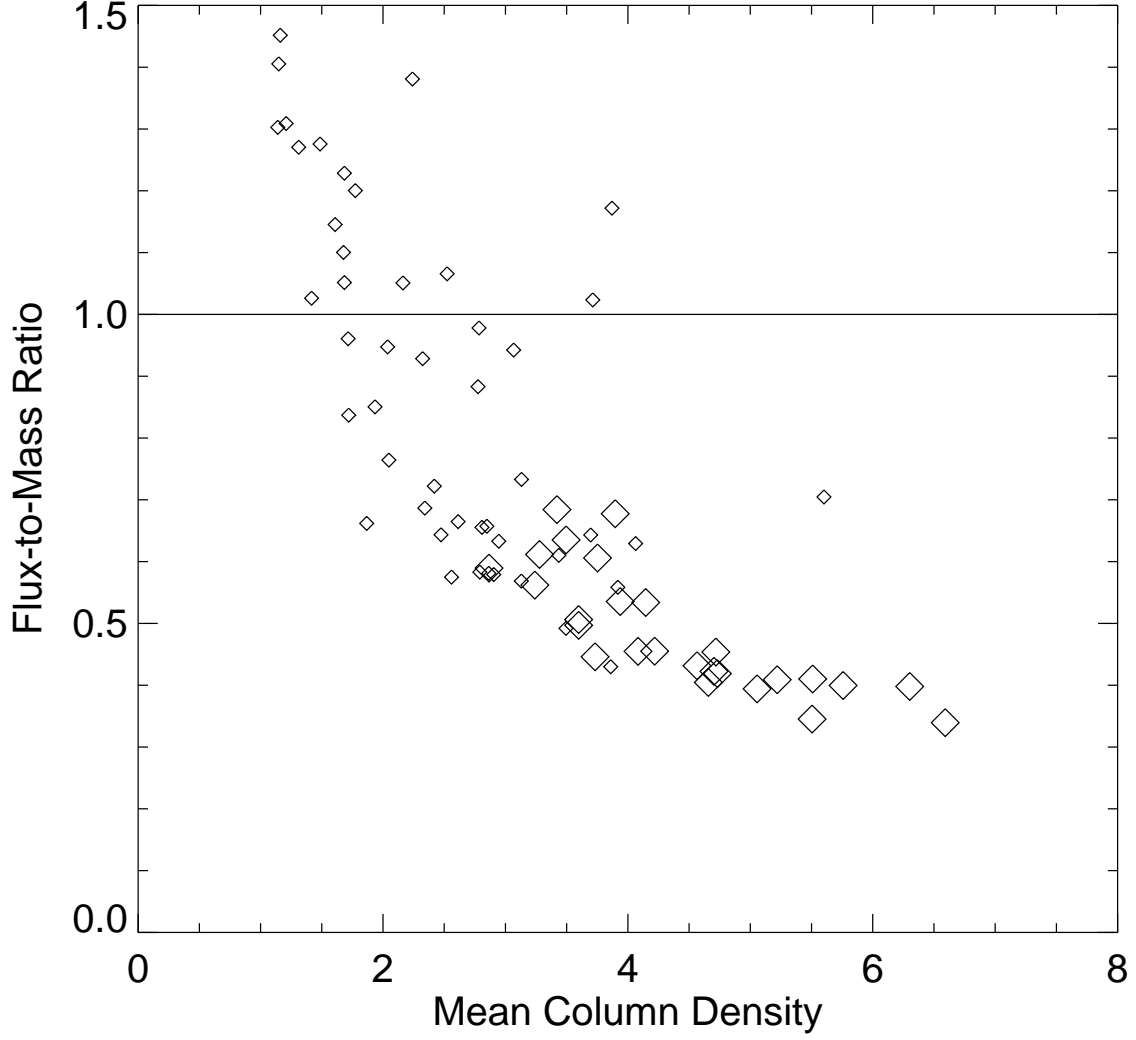


Fig. 20.— The magnetic flux-to-mass ratio as a function of the column density of the core. The large and small symbols are the same as those of Figure 15. The cores below the solid line $\Gamma_c = 1$ are magnetically supercritical. The flux-to-mass ratio tends to be smaller for more massive cores.

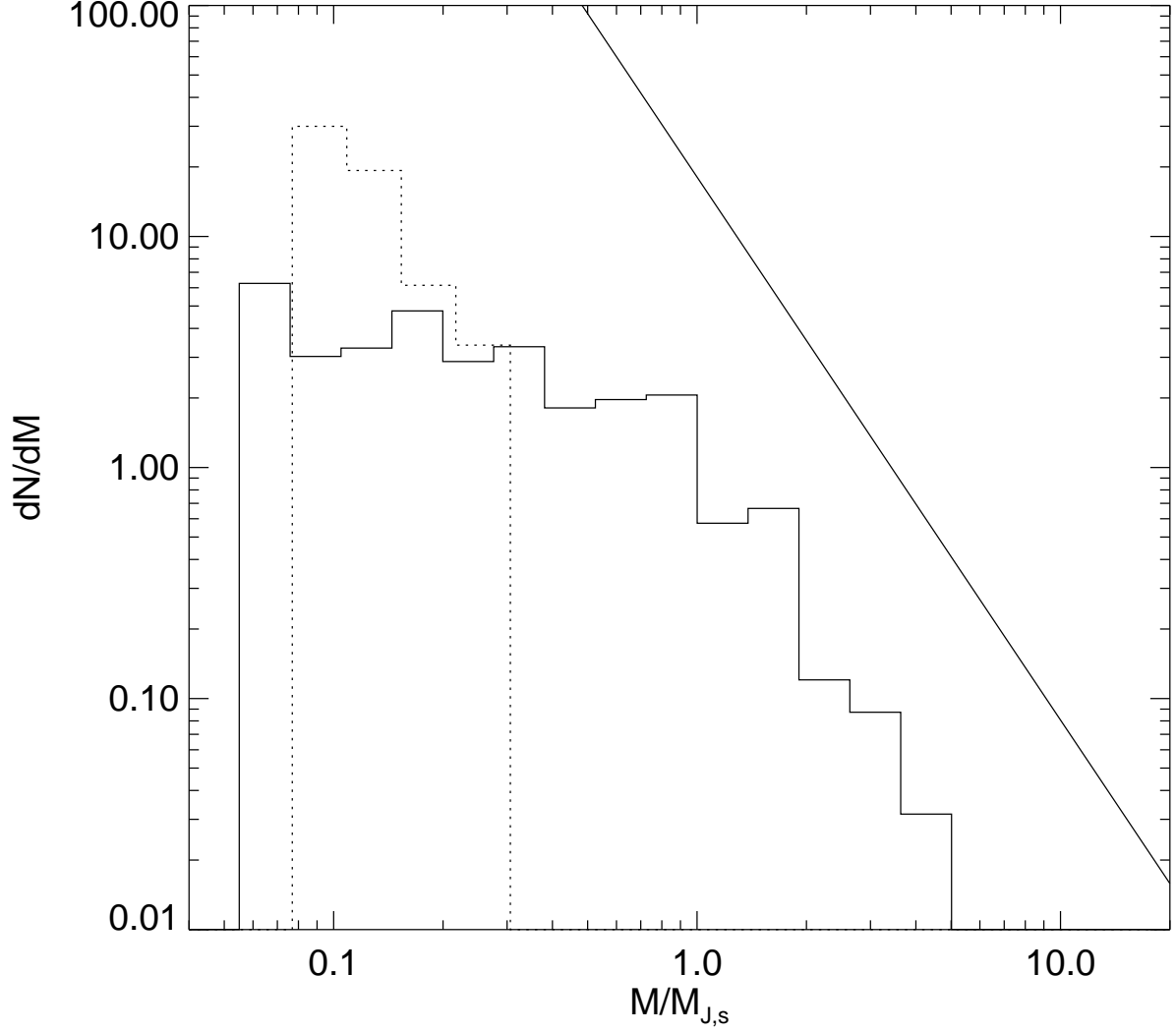


Fig. 21.— Core mass spectrum. The core mass is normalized to the Jeans mass of the Spitzer sheet, $M_{J,s}$. The solid histogram indicates the mass spectrum of dense cores. For comparison, we show the stellar mass spectrum with the dotted histogram. The solid line denotes the power law $dN/dM \propto M^{-2.35}$, the Salpeter IMF. There is a prominent break around $1M_{J,s}$ in the core mass spectrum. Above the break, the spectrum is in good agreement with the Salpeter IMF. The stellar mass spectrum can be also fitted by the Salpeter IMF.

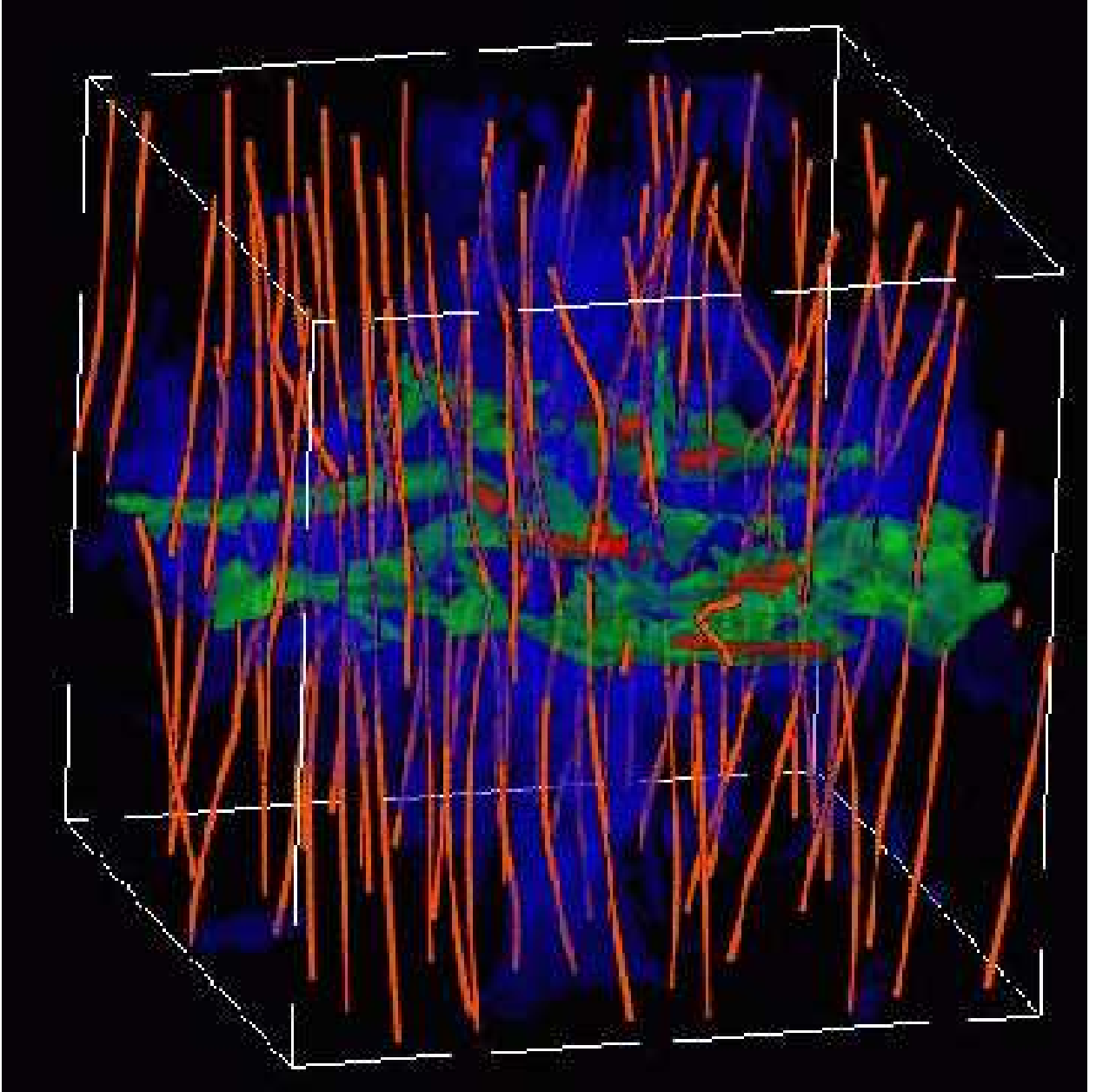


Fig. 22.— 3D view of density distribution and field lines of the standard model at the same time as in Figs. 2 and 3. The isodensity surfaces have values $\rho = 0.5$ (*blue*), 15 (*green*) and $60 \rho_0$ (*red*). They represent three distinct cloud components: turbulent diffuse halo, fragmented condensed sheet, and dense cores. The sheet is nearly magnetically critical, whereas the halo and cores are significantly subcritical and supercritical, respectively.